Supplement of Atmos. Chem. Phys., 24, 725–744, 2024
https://doi.org/10.5194/acp-24-725-2024-supplement

Atmospheric Chemistry and Physics
Open Access

Supplement of

The high-resolution Global Aviation emissions Inventory based on ADS-B (GAIA) for 2019–2021

Roger Teoh et al.

Correspondence to: Marc E. J. Stettler (m.stettler@imperial.ac.uk)

Contents

S1 Air Traffic Dataset

S1.1 Background information

Aircraft that are equipped with an ADS-B transponder broadcast their precise location at a rate of twice per second (ICAO, 2021a), and the following information is provided for each data point:

- unique aircraft identifier, which includes the International Civil Aviation Organization (ICAO) 24-bit aircraft address and call sign,
- GPS position (longitude and latitude),
- barometric altitude,
- aircraft heading, and
- timestamp when the ADS-B signal is received.

For the purposes of this research, we purchased an aircraft activity dataset from Spire Aviation (n.d.) that contains global coverage of aircraft ADS-B telemetry data from 2019 to 2021 that contains the variables listed above. Spire Aviation collects these ADS-B signals using a combination of terrestrial receivers and its own satellite constellation, where ADS-B signals from terrestrial receivers were provided at a temporal resolution of 300 s. The raw ADS-B data is subsequently enriched by Spire Aviation with third-party aircraft database sources and flight schedules to include additional flight-level information such as the:

- International Air Transport Association (IATA) flight number,
- aircraft tail number,
- ICAO aircraft type designator,
- ICAO airport code for the origin and destination airports, and
- scheduled and estimated departure and arrival time.

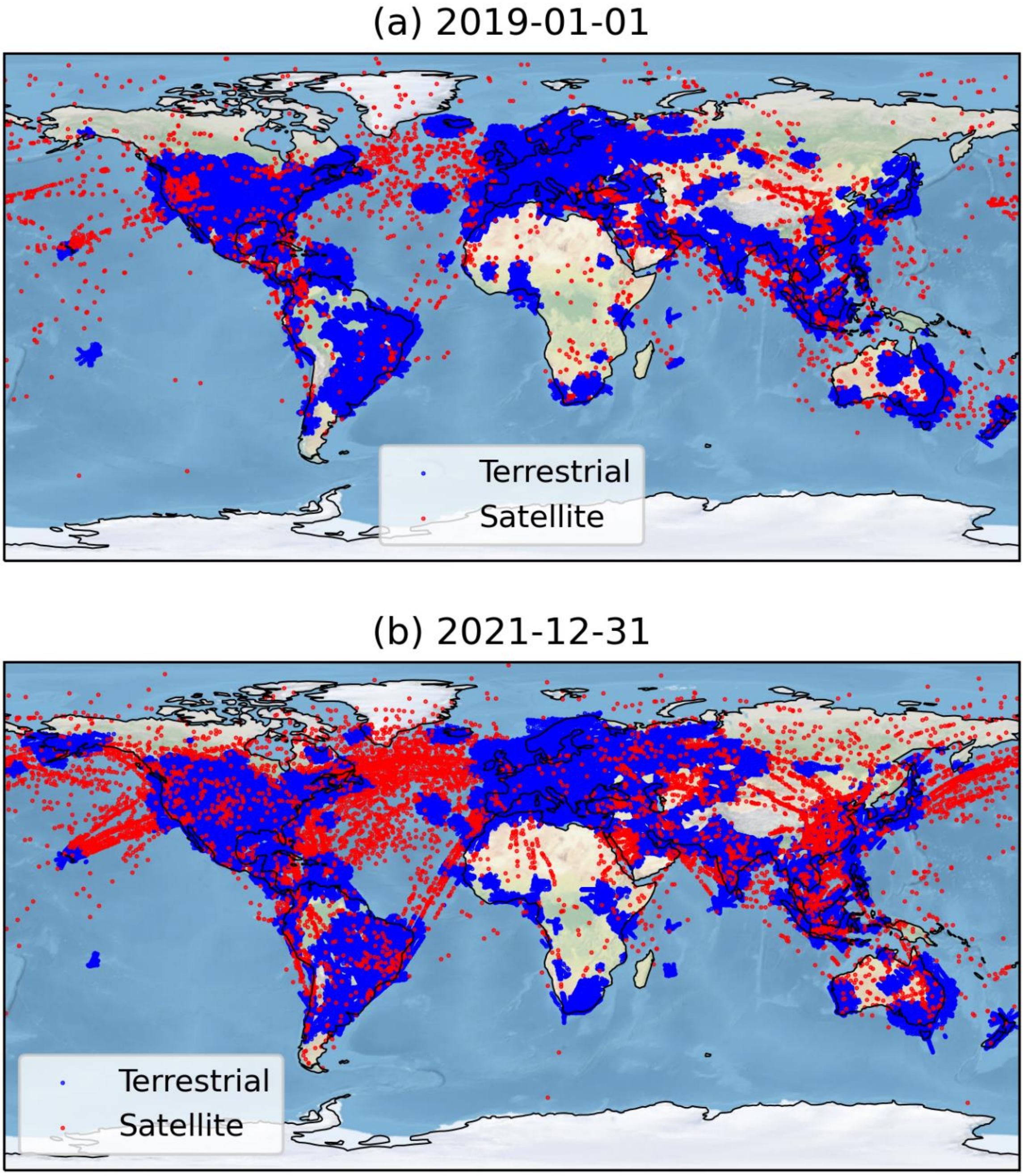

Figure S1: Aircraft GPS positions that are provided by the ADS-B dataset on the (a) 1-January-2019; and (b) 31-December-2021. Data points that are collected by terrestrial and satellite receivers are marked in blue and red respectively. Basemap plotted using Cartopy 0.21.1 © Natural Earth; license: public domain.

The aircraft activity dataset, hereby known as the ADS-B dataset, was selected ahead of other ADS-B providers (such as Flightradar24, FlightAware and the OpenSky network) because of the availability of satellite coverage and price affordability. Fig. S1 presents the aircraft GPS positions that are provided by the ADS-B dataset on 1-January-2019 and 31-December-2021, showing that: (i) satellite-based ADS-B receivers enables flights to be tracked in regions that previously had minimal radar coverage, for example, over the oceans, deserts, and mountain ranges; and (ii) an increasing coverage area of ADS-B receiver networks over time.

We also use the aircraft GPS position (longitude and latitude) provided by the ADS-B telemetry to calculate the segment length between waypoints. The ground speed (GS) is estimated by dividing the segment length by the time elapsed between waypoints, and a Savitzky-Golay filter is used to reduce the noise in the derived GS (Savitzky and Golay, 1964). The smoothed GS is subsequently converted to true airspeed (TAS) using the historical wind fields provided by the European Centre for Medium-Range Weather Forecast (ECMWF) ERA5 high-resolution realisation (HRES) reanalysis (ECMWF, 2021; Hersbach et al., 2020),

$$\mathrm{TAS} = \sqrt{(\mathrm{GS}\cos(\alpha) - U_{\mathrm{ERA5}})^2 + (\mathrm{GS}\sin(\alpha) - V_{\mathrm{ERA5}})^2}, \tag{S1}$$

where U_{ERA5} and V_{ERA5} are the eastward and northward winds at each waypoint that is estimated by performing a quadrilinear interpolation against the 4D wind fields provided by the ERA5 HRES, and α is the angle between the flight segment and the longitudinal axis. The Mach number (Ma) is then computed for each waypoint,

$$\mathrm{Ma} = \frac{\mathrm{TAS}}{\sqrt{\kappa R T}}, \tag{S2}$$

where κ (1.4) is the adiabatic index of air, R (287.05 m^2 K^{-1} s^{-2}) is the gas constant of dry air, and T is the ambient temperature (in units of K) that is provided by the ERA5 HRES.

S1.2 Data cleaning and trajectory completion

The ICAO 24-bit aircraft address and call sign are used to identify unique flights in the ADS-B tracking data. It is not possible to identify the unique trajectories from individual flights using the raw ADS-B data because multiple unique flights can share the same identifier and/or can be airborne at the same time in rare instances. Here, we develop a workflow to: (i) identify the presence of multiple unique flights with the same ICAO address/call sign; (ii) group the waypoints that belong to distinctive flights to construct their trajectories for fuel consumption and emissions modelling; and (iii) fill any missing flight segments whenever possible. Fig. S2 summarises the workflow that is developed to process the raw ADS-B dataset.

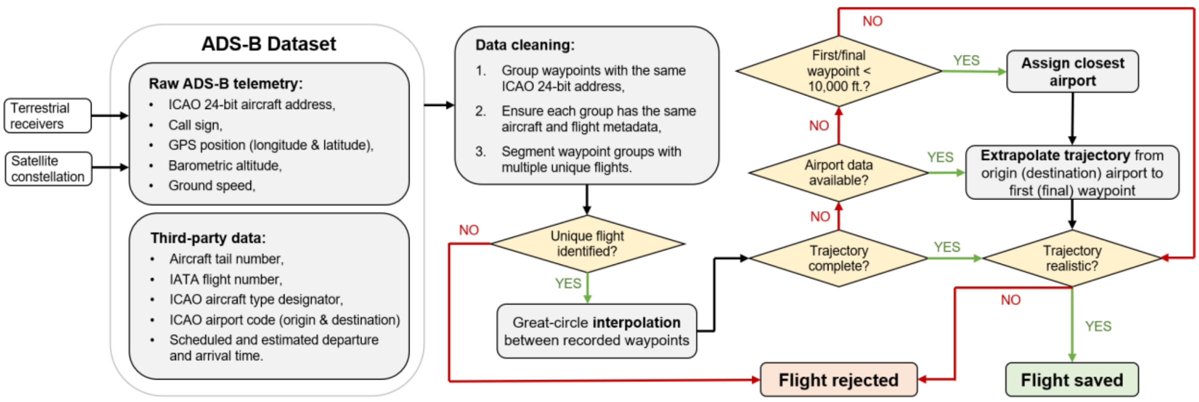

Figure S2: Data cleaning and trajectory completion workflow that is used to process the raw ADS-B dataset.

The first step involves grouping waypoints by their ICAO 24-bit address. For each group, the number of unique flights (n) are identified when the set of waypoints have more than one unique call sign, aircraft type, origin-destination airport pair, and/or tail number. If $n > 1$, the waypoints are segmented to n sub-groups so that each subgroup have the same aircraft and flight properties. The subgroup of waypoints with missing, anonymised and/or unidentifiable aircraft types, such as rotorcraft and/or sensitive military flights, are beyond the scope of this study and removed from the database. For each subgroup of waypoints, the algorithm performs additional tests with the following rules to ensure that the constructed flight trajectories are realistic:

1. the flight trajectory must consist of at least three recorded waypoints,
2. if airport metadata is available, the total flight segment length of the recorded waypoints must be greater than 5% of the distance between the origin-destination airport pair,

3. the segment length between recorded waypoints must not be greater than the great-circle distance between the origin-destination airport, or greater than 5000 km if the airport data is not available,
4. the time difference between recorded waypoints (dt) must not be greater than the time required to travel the great-circle distance between the origin-destination airport (assuming a mean cruise speed of 180 m s^{-1} for jet aircraft and 70 m s^{-1} for turboprops and piston aircraft), or greater than 6 h if the airport data is not available,
5. the estimated ground speed between waypoints must be within a reasonable range of 100–350 m s^{-1} when the flight is above 10,000 feet, or 20–300 m s^{-1} when the flight is below 10,000 feet,
6. check the altitude of waypoints during the cruise phase of flight, defined when the altitude is above 50% of the service ceiling altitude of the aircraft type and the rate of climb and descent (ROCD) is between ± 250 feet per minute. Unless there is a flight diversion, waypoints between the beginning and end of the cruise phase of flight should not be below 10,000 feet. For flights without a cruise phase of flight, the total flight duration must not be greater than 2 h, which is used as an indication that it could be a short-haul flight.

The subset of waypoints that violate conditions (1) and (2) are rejected as there is insufficient data to construct a flight segment and trajectory. Multiple unique flights are identified when conditions (3), (4), (5) and/or (6) are violated, and the waypoints are segmented at the flagged waypoints. For condition (6), the presence of flight diversion is identified when all of the following three conditions are satisfied:

- for flagged waypoints that should be at cruise (< 10,000 feet between the beginning and end of the identified cruise phase of flight), their respective dt must be less than the minimum aircraft turnaround time (i.e., duration between landing and take-off for a new flight) that is set at 10 minutes,

- the segment length between the flagged waypoints must be greater than 1 km, which indicates that the aircraft is airborne during this period, and
- the time elapsed between the flagged waypoints with the lowest altitude and the final recorded waypoint should be less than 2 h.

Fig. S3 provides an example of multiple unique flights sharing the same call sign in the raw ADS-B dataset, and the data cleaning algorithm successfully identified and segmented the waypoints into three distinctive flights. Around 90% of the waypoints have a dt < 300 s when the aircraft is within the coverage of terrestrial receivers, but dt can be up to 40000 s (~11 h) when satellite data is not available (Fig. S4). For fuel consumption, emissions, and contrail modelling, a smaller dt is necessary to account for variations in ambient meteorology and aircraft performance over large length scales. On this basis, we perform a great-circle interpolation between the recorded waypoints to produce comparable segment lengths with dt ranging between 40 and 60 s and recompute the TAS and Mach number at each waypoint. The great-circle interpolation also explicitly accounts for differences in altitude between the recorded waypoints. When the altitude between two successive waypoints is not equal and the absolute ROCD between waypoints is within ± 500 feet per minute (indicative of shallow climb/descent) (Dalmau and Prats, 2017), we assume that the aircraft performs: (i) a step climb (descent) at the start (end) of the segment when dt ≤ 0.5 h; or (ii) a step climb/descent at the mid-point when the segment length is large, identified when dt > 0.5 h. When the difference in altitude is large (absolute ROCD > 500 feet per minute) (Dalmau and Prats, 2017), we use a linear interpolation to represent a continuous climb/descent between the recorded waypoints. In rare instances where the altitude between two waypoints is below 50% of the service ceiling altitude for long time periods (dt > 1 h), i.e., no information is available during the cruise phase of flight, we assume that the aircraft will climb and cruise at ~80% of the service ceiling altitude that is rounded to the nearest flight level, and then descent to the next recorded waypoint. We note that the incorporation of step climbs/descents at cruise altitudes is necessary to ensure that the interpolated trajectories conform to the airspace design and air traffic management constraints in the real-world (Dalmau and Prats, 2017) (Fig. S5). The availability of satellite ADS-B coverage also improves the accuracy of the lateral and vertical profile of the interpolated flight trajectories (Fig. S6a). We note that the temporal resolution between waypoints that is provided by the ADS-B dataset (~300 s) might not be sufficient in capturing the full flight trajectory in the Terminal Radar Approach Control (TRACON), especially when flights are in a holding pattern, and the great-circle interpolation between recorded waypoints would likely underestimate the flight distance flown during the landing and take-off (LTO) phase of flight.

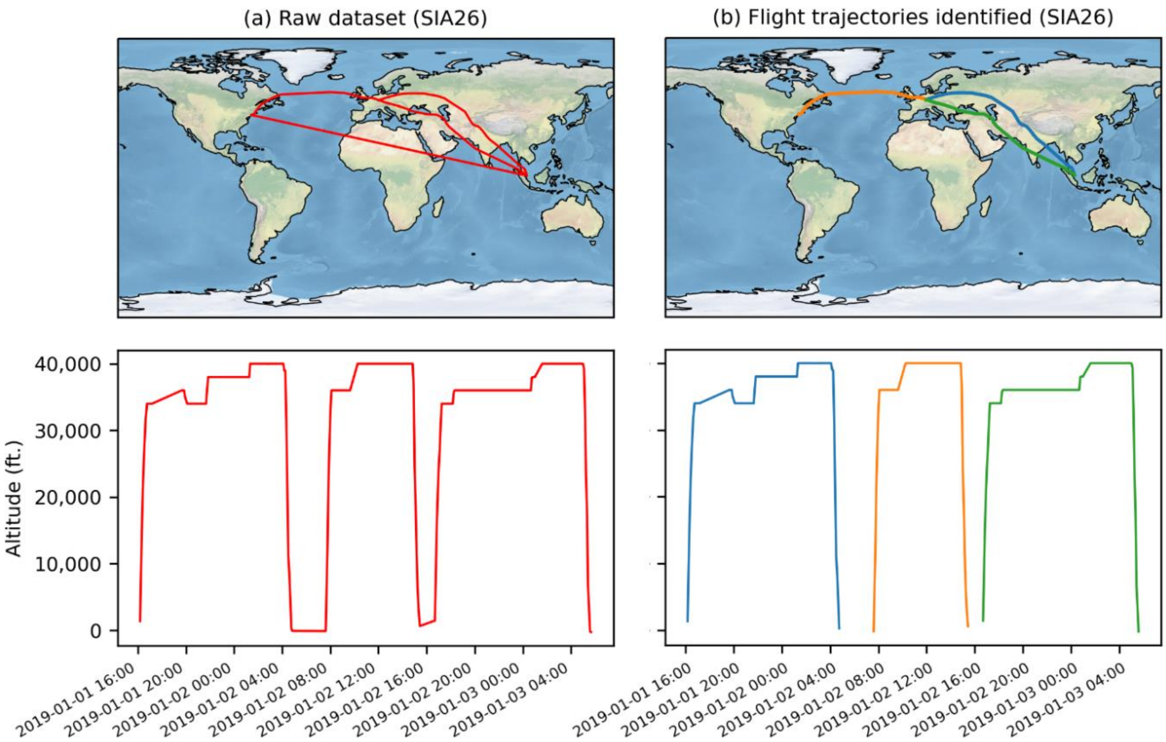

Figure S3: Example of (a) multiple unique flights sharing the same call sign in the unprocessed ADS-B dataset; and the (b) segmented trajectories into three distinctive flights. The call sign, SIA26, is used for the Singapore – Frankfurt – New York route that is operated by Singapore Airlines. Basemap plotted using Cartopy 0.21.1 © Natural Earth; license: public domain.

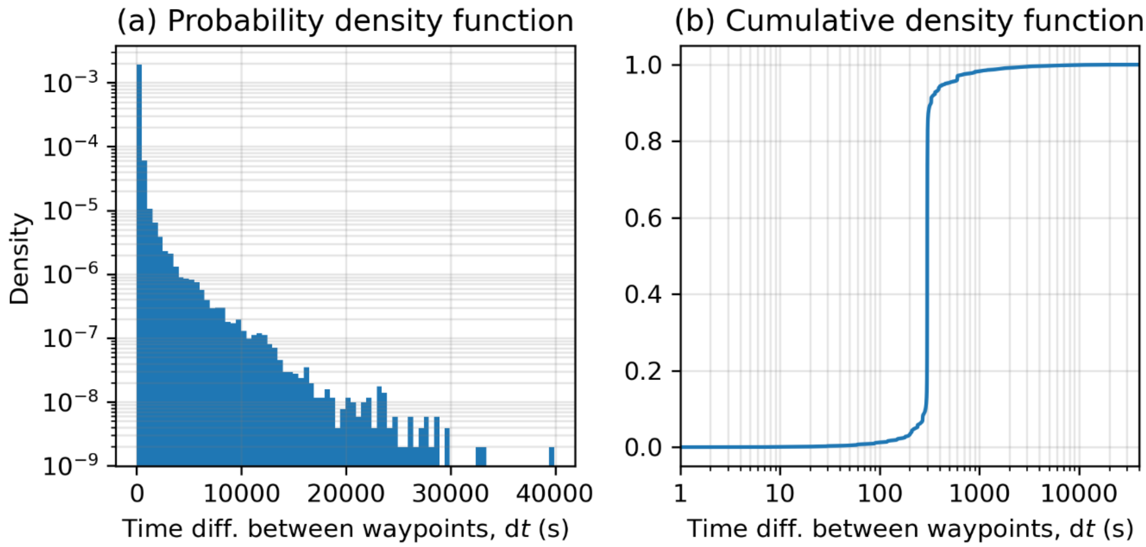

Figure S4: The (a) probability density function and (b) cumulative density function on the time difference between recorded waypoints (d*t*) in the raw ADS-B dataset.

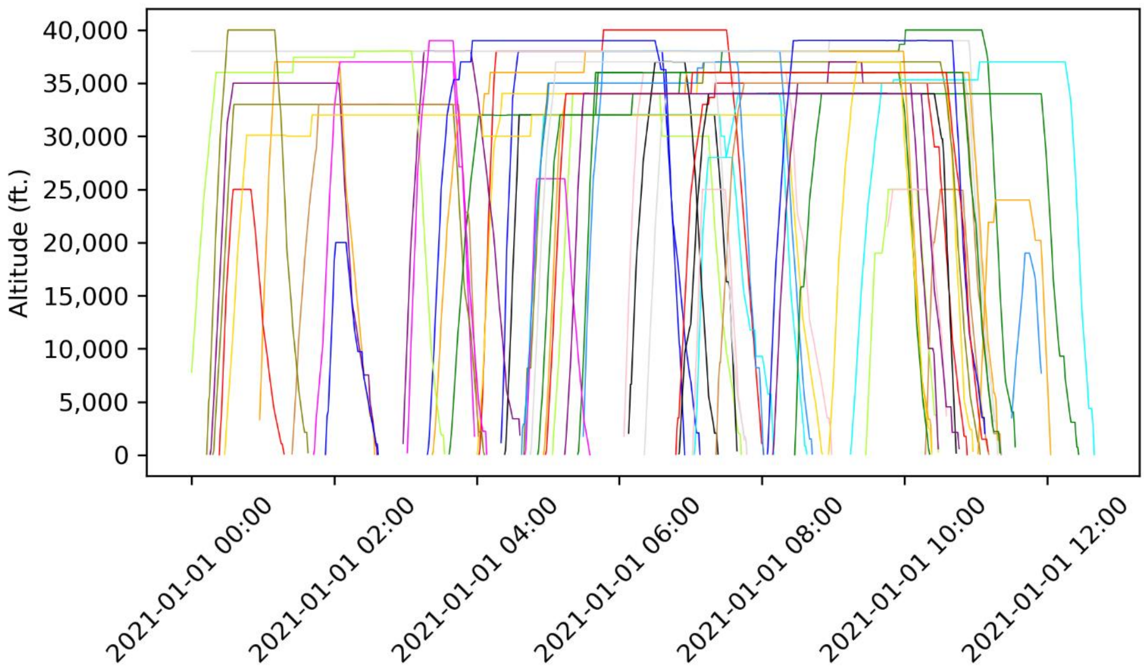

Figure S5: Vertical profile of the interpolated trajectories from 50 unique flights selected at random, where each line represents the trajectory of one unique flight.

Fig. S5 also shows that the trajectories for a subset of flights are incomplete, where the first waypoint does not start at the origin airport, and/or the final waypoint does not end at the destination airport. Whenever possible, we complete the flight trajectories using one of the two approaches: (i) a great-circle path is used to extrapolate the flight trajectory from the origin (destination) airport to the first (final) waypoint if the airport metadata is provided by the ADS-

B dataset; and (ii) if airport data is not available and the first/final waypoint is below 10,000 feet, we assign and extrapolate the flight trajectory to the nearest airport. Fig. S6b provides an example where the missing flight segment from the origin airport to the first recorded waypoint is completed when the airport metadata is available.

Additional quality checks are then performed on each of the completed flight trajectory to ensure its validity:

1. the total length of the extrapolated flight segments, i.e., distance from the origin airport to first waypoint plus the final waypoint to destination airport, must be less than 90% of the distance between airports, and
2. if the first (final) waypoint is below 50% of the service ceiling altitude, the duration of the extrapolated flight segments from the origin airport (final waypoint) to the first waypoint (destination airport) must be less than 0.5 h,
3. the completed flight trajectory must have a realistic flight time (up to 20 h). For each flight, the maximum flight time is estimated by assuming that the aircraft operates at a mean speed of 200 m s^{-1} (~700 km h^{-1}) for jet aircraft and 70 m s^{-1} (~250 km h^{-1}) for turboprops and piston aircraft, and multiplied by a tolerance factor of between 1.2 (long-haul flights) and 2.5 (short-haul) depending on the time difference between the first and final recorded waypoint, and
4. the segment length between successive waypoints must be realistic. The maximum segment length between waypoints is estimated by multiplying dt with an assumed mean speed (200 m s^{-1} or ~700 km h^{-1} for jet aircraft, and 70 m s^{-1} ~250 km h^{-1} for turboprops and piston aircraft), and a tolerance factor of 2 is added.

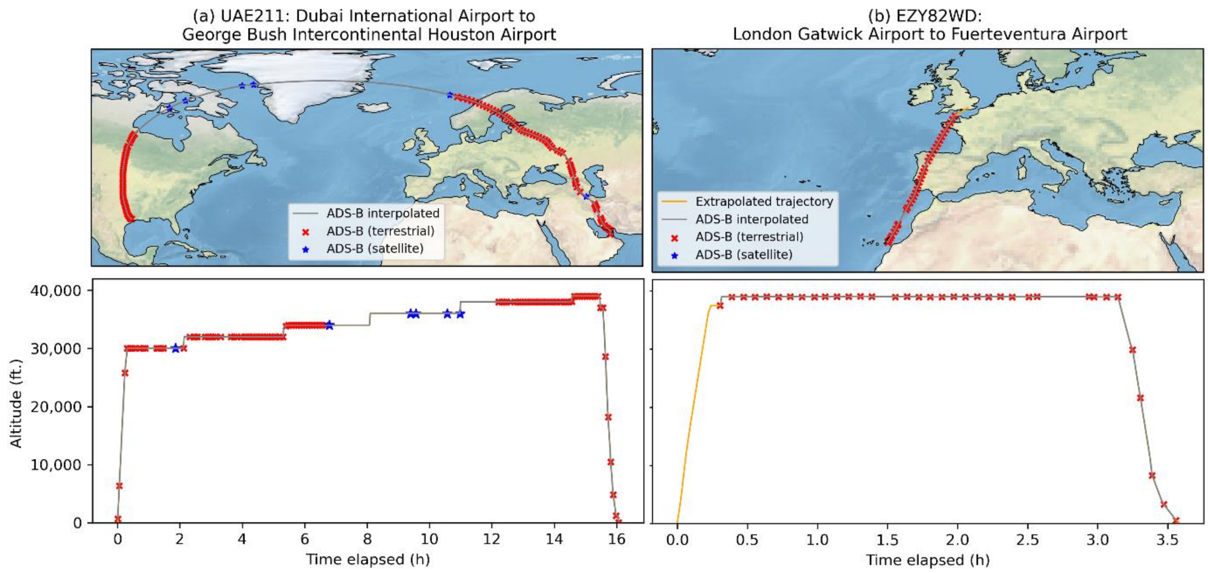

Figure S6: The interpolated lateral (top) and vertical (bottom) trajectory from two example flights. Basemap plotted using Cartopy 0.21.1 © Natural Earth; license: public domain.

Flights that violate Condition (2) are likely caused by upstream errors in linking the call sign and flight schedule database to obtain the airport metadata, and we replace the flight trajectory by assuming a great-circle path between the given origin-destination airports (1.5% of all flights). Flights that violate Conditions (1), (3) and/or (4) are generally indicative of the trajectory containing erroneous waypoints and are rejected.

S1.3 Summary statistics & validation

Fig. S7 presents the summary statistics for the cleaned ADS-B dataset and shows that:

- 103.7 million flight trajectories are recorded between 2019 and 2021 (Fig. S7a),
- 75.2% of all flights are carried out by jet aircraft, 9.4% by turboprops, and the remaining 15.4% by piston aircraft (Fig. S7b),
- origin and destination airport metadata are available for 79.1% of all flights, and this figure increases to 90.9% when piston aircraft, mostly used in general aviation, are excluded (Fig. S7c),

- 67.4% of all flights have full trajectory coverage, i.e., first waypoint starting from the origin airport and ending at the destination airport, and this figure increases to 77.6% when piston aircraft are excluded (Fig. S7d),
- 5.0% of all flights are rejected from the ADS-B dataset (Fig. S7e), and
- at the waypoint level, 99.5% of the recorded ADS-B signals are from terrestrial receivers and the remaining 0.5% are provided by satellite receivers (Fig. S7f).

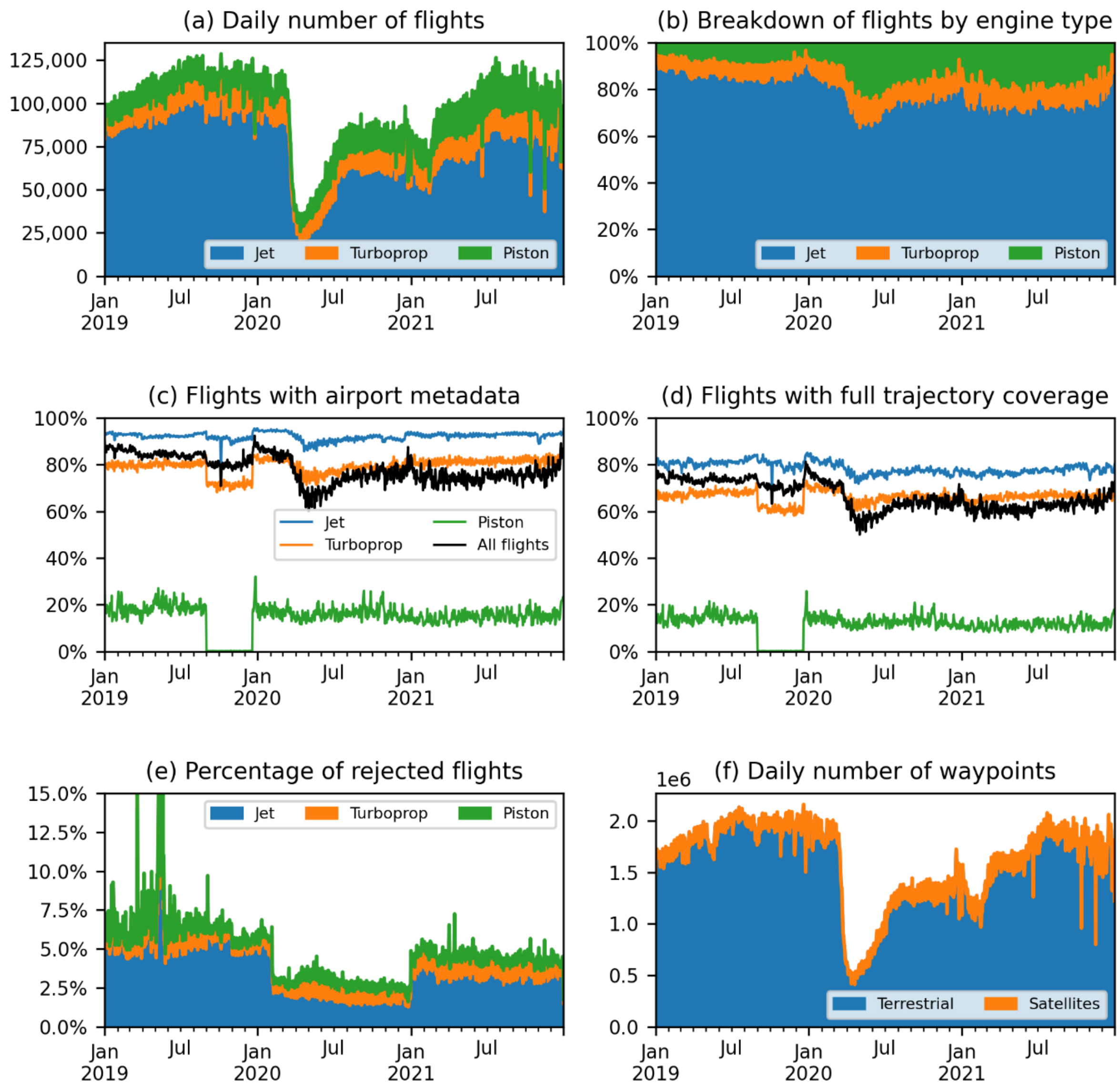

Figure S7: Summary statistics of the cleaned ADS-B dataset, showing the (a) daily number of flights globally; (b) breakdown of flights by engine type; (c) percentage of flights with origin-destination airport metadata; (d) percentage of flights with full trajectory coverage; (e) percentage of rejected flights due to unrealistic flight time and/or segment length; and (f) daily number of waypoints.

Table S1: Comparison of the global annual number of flights from the cleaned ADS-B dataset versus statistics published by ICAO and IATA.

	ADS-B dataset: Total number of flights (millions)		ICAO & IATA: Number of departures from scheduled services (million)	Difference[a]
	All flights	Jet and turboprop		
2019	40.2	36.5	38.3	-4.7%
2020	27.9	23.0	20.3	+13.3%
2021	35.6	28.2	24.1[b]	+17.0%

[a]: Difference in the total number of jet and turboprop flights in the ADS-B dataset relative to ICAO & IATA.

[b]: Extrapolated using preliminary statistics published by IATA (2022a).

Table S2: Comparison of the global annual flight distance flown that is derived from the cleaned ADS-B dataset versus estimates from produced by Airlines for America.

	Total flight distance flown (x10^9 km)			Difference*
	ADS-B: All flights	ADS-B: Jet and turboprop	Airlines for America	
2019	60.9	60.3	56.2	+8.4%
2020	34.5	33.7	28.0	+23.2%
2021	41.9	40.8	33.7	+24.3%

*: Difference in the total flight distance flown from jet and turboprop flights in the ADS-B dataset relative to Airlines for America (2022).

The 5% of all flights that are rejected from the ADS-B dataset are caused by identified errors in their respective flight trajectories, for example,

- trajectories that contain less than three waypoints (56.6% of all rejected flights),
- trajectories with very long extrapolated segment lengths, i.e., > 90% of the distance between the origin-destination airport (20.6% of all rejected flights),
- flights with unrealistic flight time (13.3% of all rejected flights), and
- flight segments with unrealistic ground speed (9.5% of all rejected flights).

To assess the completeness of the processed ADS-B dataset, we compared the: (i) global annual number of flights with statistics published by ICAO and IATA (ICAO 2019, 2020, 2021b; IATA, 2022a), which counts the number of departures from scheduled flights; and (ii) global annual flight distance flown with estimates provided by Airlines for America (2022), which captures the air traffic activity from passenger and cargo airline operations. As these datasets only include the air traffic activity from scheduled/commercial flights, we only include flights that are performed by jet and turboprop aircraft in the ADS-B dataset. Flights that arise from general aviation, which are identified by those performed by piston aircraft, are excluded from the comparison.

The comparison with statistics from ICAO and IATA (Table S1) shows that the number of jet and turboprop flights captured by the ADS-B dataset in 2019 (36.5 million) is ~4.7% lower than the global statistics (38.3 million), and this is likely caused by: (i) the smaller global coverage area of ADS-B receiver networks in 2019 relative to 2021 (Fig. S1), where the subset of flights outside the coverage area might not be recorded; and (ii) of the presence of erroneous trajectories in the raw ADS-B dataset in 2019, where 6.6% of flights being rejected because the validity of their trajectories cannot be verified (Fig. S7e). The ADS-B dataset captured a higher number of jet and turboprop flights relative to the ICAO and IATA statistics in 2020 (23.0 vs. 20.3 million, +13%) and 2021 (28.2 vs. 24.1 million, +17%), and these discrepancies could be due to the change in the proportion of unscheduled flights, i.e., charter flights, cargo services and private aviation, which increased from 4.1% in 2019 to 7.5% in 2020 (Sobieralski and Mumbower, 2022; ICAO, 2021b). Notably, the global annual flight distance flown from jet and turboprop aircraft in the ADS-B dataset are around 8–24 % higher when compared to estimates produced by Airlines for America (Table S2), and this could be because Airlines for America: (i) only accounts for the flight distance flown from passenger and cargo airline operations; and (ii) estimated the flight distance flown based on scheduled activity and likely assumed a great-circle path between the origin-destination airport with a lateral inefficiency factor.

In addition to the global statistics, we also compared the number of air traffic movements derived from the ADS-B dataset with official traffic statistics published by London Heathrow Airport (ICAO airport code: EGLL) (Heathrow Airport, 2022), New York John F. Kennedy International Airport (KJFK) (Port Authority of New York and New Jersey, 2022), and

Singapore Changi Airport (WSSS) (Changi Airport Group, 2020, 2022; Singapore Airport, 2022). Fig. S8 shows that the total number of aircraft movements derived from the processed ADS-B dataset can be between 1–7% lower when compared with published statistics from the three airports (-1.3% for EGLL, -7.0% for KJFK and -1.3% for WSSS between 2019 and 2021). For the comparison with WSSS, we note that the published data does not include air traffic movements from freight operations and private aviation, and therefore, the monthly number of flights in the ADS-B dataset can be higher than the published statistics.

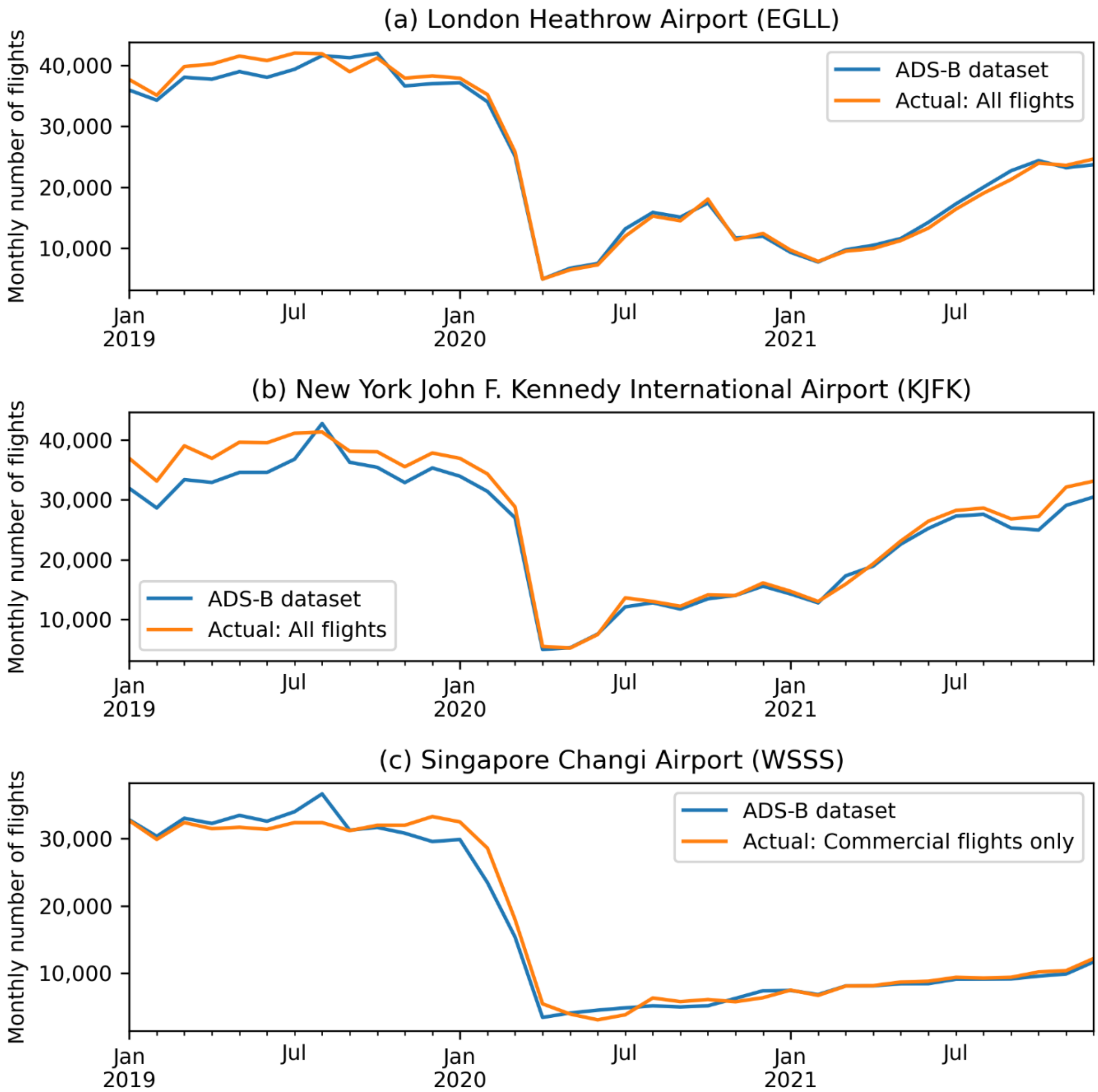

Figure S8: Comparison of the monthly number of air traffic movements derived from the ADS-B dataset relative to published traffic statistics from: (a) London Heathrow Airport; (b) New York John F. Kennedy International Airport; and (c) Singapore Changi Airport.

S2 Aircraft-engine combination

Fig. S9 provides a breakdown of the 2019–2021 global fleet composition in the ADS-B dataset by their ICAO aircraft type designator. We note that the same ICAO aircraft type designator can consist of multiple aircraft variants that are powered by different engine types. For example, the "A320" ICAO aircraft type designator covers the A320-212, A320-214, A320-231, and A320-232 variants, and these variants can either be powered by the IAE V2500 or CFM56-5 engine series. The aircraft variant is used by the Base of Aircraft Data Family 4 (BADA 4) aircraft performance model to simulate the fuel consumption (EUROCONTROL, 2016), while the specific engine model is required by the ICAO Aircraft Engine Emissions Databank (EDB) (EASA, 2021) to estimate the emission indices (EI) of nitrogen oxide (NO_X), carbon monoxide (CO), unburnt hydrocarbons (HC) and non-volatile particulate matter (nvPM) for each flight.

To obtain this information, we utilise a global fleet database from a commercial company (Cirium) to link the registered aircraft tail number to the specific aircraft variant and engine model (Cirium, 2022). The fleet database covers around 59% of all flights in the ADS-B dataset or 79% of all flights that are carried out by jet aircraft. Table S3 provides a breakdown of engine market share for the commonly used passenger aircraft types for flights that are covered by the fleet database. For the remaining flights not covered by fleet database, we assign the default aircraft-engine combination using the Base of Aircraft Data (BADA) database (Table S4) with modifications applied to the A320 (replaced V2500-A1 with CFM56-5B4), B788 (Trent 1000-A → GEnX-1B70/P2) and B789 (Trent 1000-J → GEnX-1B75/P2) to use the engine type with the highest market share (shown in Table S3).

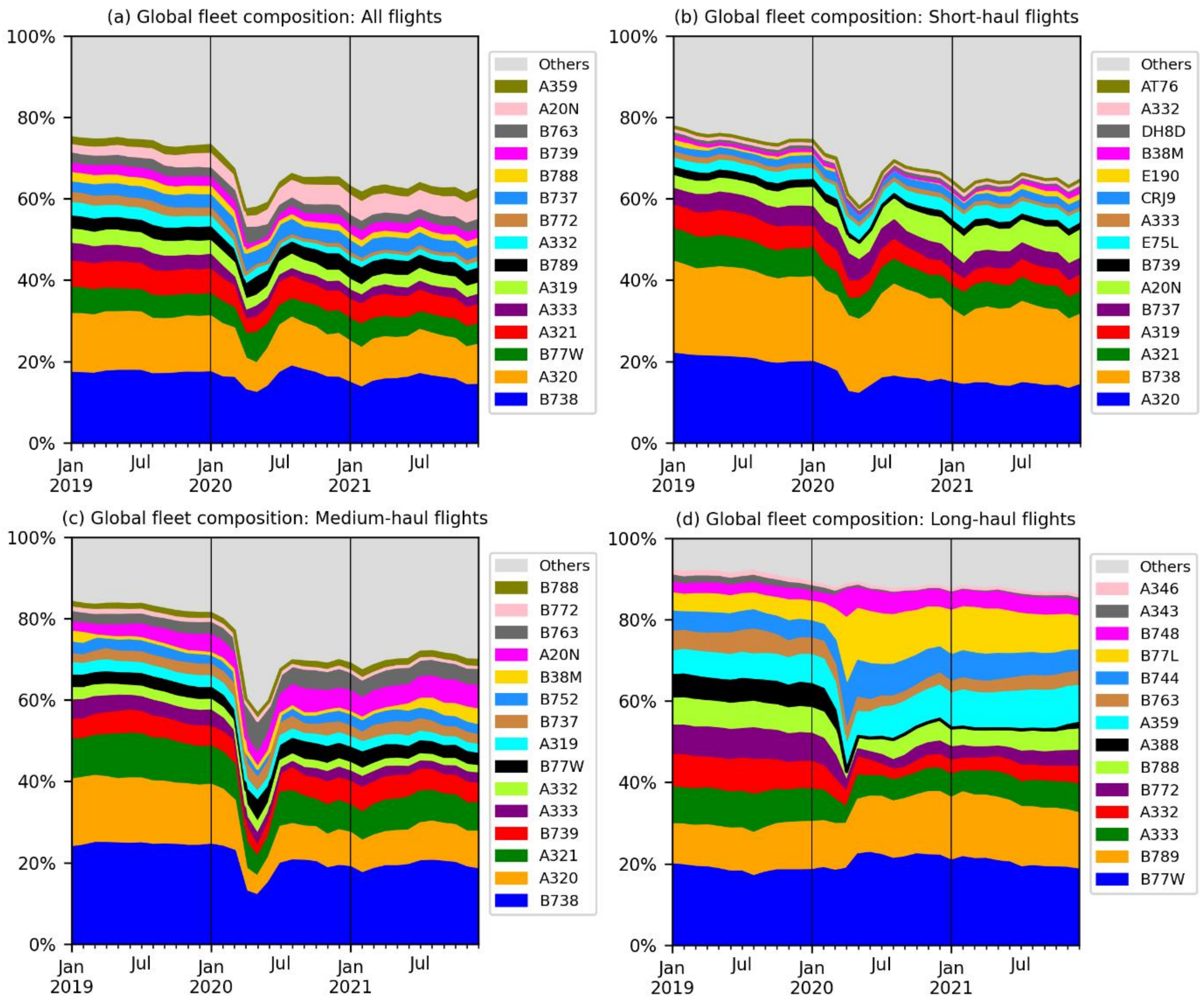

Figure S9: Global fleet composition by distance travelled for: (a) all flights; (b) short-haul flights ($t \leq 3$ h); (c) medium-haul flights ($3 < t < 6$ h); and (d) long-haul flights ($t > 6$ h) in the ADS-B dataset between 2019 and 2021.

Table S3: Breakdown of the engine market share for 23 commonly used passenger aircraft types in the ADS-B dataset by flight distance travelled. Flights are only included in this analysis if the registered aircraft tail number is available in the fleet database.

ICAO aircraft type designator	Engine Name	Engine UID - ICAO EDB	Market share (%)		
			2019	2020	2021
A319	CFM56-5B5/3	01P08CM106	30%	21%	21%
	CFM56-5B6/3	01P08CM107	25%	23%	23%
	CFM56-5B7/3	01P08CM108	9%	18%	17%
	V2522-A5	01P10IA019	11%	10%	8%
	V2524-A5	01P10IA020	22%	22%	25%
	V2527-A5M	01P10IA023	4%	7%	6%
A320	CFM56-5B4/3	01P08CM105	52%	55%	56%
	CFM56-5B6/3	01P08CM107	7%	4%	3%
	V2527-A5	01P10IA021	38%	38%	38%
	V2527-A5E	01P10IA022	3%	3%	4%
A321	CFM56-5B1/3	01P08CM102	2%	1%	1%
	CFM56-5B2/3	01P08CM103	2%	3%	3%
	CFM56-5B3/3	01P08CM104	33%	35%	37%
	V2530-A5	01P10IA024	3%	2%	2%
	V2533-A5	01P10IA025	60%	58%	57%
A19N	LEAP-1A26CJ	01P20CM129	100%	100%	100%
A20N	LEAP-1A26/26E1	01P20CM128	59%	55%	53%
	PW1127G-JM	01P18PW153	39%	43%	46%
	PW1127GA-JM	01P18PW152	2%	2%	2%
A21N	LEAP-1A35A/33/33B2/32/30	01P20CM132	40%	39%	43%
	PW1130G-JM	01P18PW155	7%	7%	3%
	PW1133GA-JM	01P18PW156	2%	4%	7%
	PW1133G-JM	01P18PW157	51%	51%	48%
A332	Trent 772	01P14RR102	100%	100%	100%
A333	Trent 768	01P14RR101	4%	3%	5%
	Trent 772	01P14RR102	96%	97%	95%
A346	Trent7000-72	02P23RR141	93%	100%	0%
	CFM56-5B6/3	01P08CM107	7%	0%	0%
A359	Trent XWB-75	01P18RR121	3%	5%	8%
	Trent XWB-84	01P18RR124	97%	95%	92%
A35K	Trent XWB-97	01P21RR125	100%	100%	100%
A388	Trent 970-84	01P18RR103	67%	56%	18%
	Trent 972-84	01P18RR104	12%	12%	0%
	Trent 972E-84	01P18RR105	22%	33%	82%
B737	CFM56-7B20E	01P11CM111	9%	8%	8%
	CFM56-7B22E	01P11CM112	65%	67%	68%
	CFM56-7B24E	01P11CM114	23%	23%	22%
	CFM56-7B26E	01P11CM116	3%	3%	2%

ICAO aircraft type designator	Engine Name	Engine UID - ICAO EDB	Market share (%)		
			2019	2020	2021
B738	CFM56-7B24E	01P11CM114	16%	18%	17%
	CFM56-7B26E	01P11CM116	73%	71%	72%
	CFM56-7B27E	01P11CM121	8%	8%	8%
	CFM56-7B27E/B1	01P11CM122	3%	2%	2%
B739	CFM56-7B24E	01P11CM114	3%	2%	3%
	CFM56-7B26E	01P11CM116	50%	47%	42%
	CFM56-7B27E	01P11CM121	45%	49%	54%
	CFM56-7B27E/F	01P11CM125	2%	2%	2%
B744	CF6-80C2B1F	01P02GE186	76%	70%	68%
	CF6-80C2B5F	01P03GE187	24%	30%	32%
B762	CF6-80C2B5F	01P03GE187	23%	5%	7%
	CF6-80C2B6F	01P02GE188	77%	95%	93%
B763	CF6-80C2B6F	01P02GE188	100%	100%	100%
B77L	GE90-110B1	01P21GE216	90%	95%	94%
	GE90-115B	01P21GE217	10%	5%	6%
B77W	GE90-115B	01P21GE217	100%	100%	100%
B788	GEnx-1B64/P2	01P17GE206	16%	13%	8%
	GEnx-1B67/P2	01P17GE207	11%	10%	10%
	GEnx-1B70/75/P2	01P17GE209	15%	17%	19%
	GEnx-1B70/P2	01P17GE210	27%	31%	37%
	Trent 1000-AE3	02P23RR126	2%	3%	2%
	Trent 1000-CE3	02P23RR127	7%	4%	2%
	Trent 1000-D3	02P23RR128	4%	4%	6%
	Trent 1000-G3	02P23RR129	18%	17%	16%
B789	GEnx-1B74/75/P2	01P17GE211	58%	60%	63%
	GEnx-1B76A/P2	01P17GE214	4%	6%	5%
	Trent 1000-J3	02P23RR131	34%	30%	27%
	Trent 1000-K3	02P23RR132	4%	4%	4%
B78X	GEnx-1B74/75/P2	01P17GE211	22%	23%	26%
	GEnx-1B76/P2	01P17GE213	31%	47%	43%
	GEnx-1B76A/P2	01P17GE214	6%	5%	3%
	Trent 1000-M3	02P23RR134	41%	25%	27%

Table S4: Default aircraft-engine assignment for jet aircraft if the registered aircraft tail number is not included in the fleet database. For turboprop and piston aircraft, their respective engines are not available in the ICAO EDB and a constant emissions index is used to calculate the NO_X, CO, HC and nvPM emissions.

ICAO Aircraft Code	Engine - EDB	Engine UID - EDB	ICAO Aircraft Code	Engine - EDB	Engine UID - EDB
A148	D-436-148	13ZM003	C650	TFE731-3	1AS002
A158	D-436-148	13ZM003	C680	PW306B	7PW078
A20N	PW1127G-JM	01P22PW163	C750	AE3007C	6AL022
A21N	LEAP-1A35A/33/33B2/32/30	01P20CM132	CL30	HTF7000 (AS907-1-1A)	11HN003
A306	PW4158	1PW048	CL60	CF34-3B	01P05GE189
A30B	CF6-50C2	3GE074	CRJ1	CF34-3A1	1GE035
A310	CF6-80C2A2	1GE015	CRJ2	CF34-3B1	01P05GE189
A318	CFM56-5B9	01P08CM110	CRJ9	CF34-8C5	01P08GE190
A319	V2522-A5	01P10IA019	CRJX	CF34-8C5A1	01P08GE191
A320	CFM56-5B4/3	01P08CM105	DC10	CF6-50C2	3GE074
A321	V2530-A5	01P10IA024	DC87	CFM56-2-C5	1CM003
A332	Trent 772B	01P14RR102	DC93	JT8D-11	1PW008
A333	Trent 768	01P14RR101	DC94	JT8D-11	1PW008
A339	Trent7000-72	02P23RR141	E135	AE3007A1/3	01P06AL030
A342	CFM56-5C4	2CM015	E145	AE3007A1	01P06AL028
A343	CFM56-5C4	2CM015	E170	CF34-8E5	01P08GE197
A345	Trent 553	8RR044	E190	CF34-10E6	8GE116
A346	Trent 556	6RR041	E195	CF34-10E7	8GE119
A359	Trent XWB-84	01P18RR124	E290	PW1919G	20PW134
A35K	Trent XWB-97	01P21RR125	E35L	AE 3007A1E	01P06AL032
A388	Trent 970-84	01P18RR103	E45X	AE 3007A1E	01P06AL032
A3ST	CF6-80C2A8	1GE021	E545	AS907-3-1E	01P14HN014
B38M	LEAP-1B27	01P20CM136	E550	AS907-3-1E	01P14HN015
B39M	LEAP-1B28	01P20CM140	E75L	CF34-8E5A1	01P08GE191
B462	ALF 502R-5	1TL003	E75S	CF34-8E5A1	01P08GE191
B463	ALF 502R-5	1TL003	F100	TAY Mk620-15	1RR020
B703	JT3D-3B	1PW001	F28	Spey 555	4RR035
B712	BR700-715A1-30	4BR002	F2TH	PW308C BS 1289	03P14PW194
B722	JT8D-15	1PW009	F70	TAY Mk620-15	1RR020
B732	JT8D-15	1PW009	F900	TFE731-2-2B	1AS001
B733	CFM56-3B2	1CM005	FA10	TFE731-2-2B	1AS001
B734	CFM56-5A	1CM008	FA50	TFE731-2-2B	1AS001
B735	CFM56-3	1CM004	FA7X	PW307A	03P16PW192
B736	CFM56-7B22E	01P11CM112	G150	TFE731-2-2B	1AS001
B737	CFM56-7B24E	01P11CM114	G280	AS907-2-1G (HTF7250G)	01P11HN012
B738	CFM56-7B26E	01P11CM116	GL5T	BR700-710A2-20	01P04BR013
B739	CFM56-7B27E	01P11CM121	GLEX	BR700-710A2-20	01P04BR013

ICAO Aircraft Code	Engine - EDB	Engine UID - EDB	ICAO Aircraft Code	Engine - EDB	Engine UID - EDB
B742	RB211-524D4	1RR008	GLF2	SPEY Mk511	8RR043
B743	JT9D-7R4G2	1PW029	GLF5	BR700-710C4-11	01P06BR014
B744	CF6-80C2B1F	01P02GE186	H25B	TFE731-3	1AS002
B748	GEnx-2B67	01P17GE215	HA4T	PW308A	01P07PW145
B752	RB211-535E4	1RR013	IL76	D-30KP-2	1AA002
B753	RB211-535E4-B	3RR028	IL86	NK-86	1KK003
B762	CF6-80A2	1GE012	IL96	PS-90A	1AA005
B763	PW4060	1PW043	L101	RB211-22B	1RR002
B764	CF6-80C2B6F	01P02GE188	LJ35	TFE731-2-2B	1AS001
B772	Trent 892	2RR027	LJ45	TFE731-2-2B	1AS001
B773	Trent 892	2RR027	LJ60	PW306A	7PW077
B77L	GE90-110B1	01P21GE216	MD11	PW4460	1PW052
B77W	GE90-115B	01P21GE217	MD82	JT8D-217C	4PW070
B788	GEnx-1B70/P2	01P17GE210	MD83	JT8D-219	1PW019
B789	GEnx-1B75/P2	01P17GE212	Q4	AE 3007H	8AL025
B78X	GEnx-1B76/P2	01P17GE213	RJ1H	LF507-1F, -1H	1TL004
BA11	SPEY Mk511	8RR043	RJ85	LF507-1F, -1H	1TL004
BE40	JT15D-5C	1PW038	SU95	SaM146-1S17	01P11PJ003
BER2	D-436-148 F1	13ZM004	T134	D-30 (Il series)	1AA001
C550	JT15D-4 series	1PW036	T154	D-30KU-154	1AA004
C551	JT15D-4 series	1PW036	T204	PS-90A	1AA005
C560	JT15D-5, -5A, -5B	1PW037	YK42	D-36	1ZM001

S3 Passenger Load Factor

The passenger load factor, i.e., the number of passengers divided by the aircraft seat capacity, is required to estimate the aircraft mass, c.f. Eq. (1) in the main text, which is subsequently used by BADA to estimate the thrust force and fuel consumption rate. Existing studies generally: (i) use a constant annual passenger load factor globally (Quadros et al., 2022; Wasiuk et al., 2015); or (ii) assume a nominal (reference) mass for a given aircraft type (Teoh et al., 2022a) that is provided by the BADA database (EUROCONTROL, 2019, 2016). However, the COVID-19 pandemic led to significant temporal and regional variations in the passenger load factor that needs to be accounted for (ICAO, n.d.).

Here, we compile the global (monthly) and regional (annual) passenger load factor (LF) statistics between December-2018 and January-2022 from published data by ICAO and IATA

(ICAO 2019, 2021b; 2022; IATA, 2022b) (Tables S5 and S6). As a breakdown of the monthly regional passenger LF is not available, we approximate it as a ratio of the regional and global annual LF,

$$\text{Regional LF}_{\text{month}} = \left(\frac{\text{Regional LF}_{\text{annual}}}{\text{Global LF}_{\text{annual}}}\right) \times \text{Global LF}_{\text{month}}. \quad \text{(S3)}$$

A linear interpolation relative to the monthly regional LF is then used to obtain the daily regional LF, and this approach ensures that the day-to-day passenger LF is continuous without abrupt shifts in magnitude (Fig. S10). For each flight, we assign the: (i) regional passenger LF that is based on the region of the origin airport that is identified using the first letter of the ICAO airport code (Table S7); or (ii) global mean passenger LF if airport data is not available. In real-world operations, the passenger/weight LF varies between different airlines (low-cost vs. full-service carriers), aircraft type (narrowbody vs. widebody aircraft) and mission profile (short-haul vs. long haul flights, and passenger vs. freight services). However, our approach is unable to account for these LF variabilities because of the lack of publicly available disaggregated LF data.

Table S5: Annual available seat kilometre (ASK) and passenger load factor between 2019 and 2021.

Region	ASK (% of global)			Passenger Load Factor (%)		
	2019	2020	2021	2019	2020	2021
Global	100	100	100	82.4	65.3	67.9
Europe	26.0	22.5	24.9	85.0	68.1	68.6
Africa	2.4	2.1	1.9	72.4	60.8	59.5
Middle East	9.9	9.4	6.5	75.6	59.9	51.5
Asia and Pacific	35.1	36.6	27.5	81.7	67.8	62.6
North America	21.6	24.6	32.6	84.8	59.6	73.8
Latin America and Caribbean	5.0	4.8	6.6	82.1	74.8	77.3

Table S6: Actual monthly global passenger load factor compiled using published data from ICAO (2022), and the monthly regional passenger load factor is estimated using Eq. (S3).

Month	Passenger Load Factor (%)						
	Global	Europe	Africa	Middle East	Asia & Pacific	North America	Latin America & Caribbean
Dec-2018	80.4	82.9	70.6	73.7	79.7	82.7	80.1
Jan-2019	79.6	82.1	69.9	73.0	78.9	81.9	79.3
Feb-2019	80.6	83.1	70.8	73.9	79.9	82.9	80.3
Mar-2019	81.7	84.3	71.8	74.9	81.0	84.1	81.4
Apr-2019	82.8	85.4	72.7	75.9	82.1	85.2	82.5
May-2019	81.5	84.1	71.6	74.8	80.8	83.9	81.2
Jun-2019	84.4	87.0	74.1	77.4	83.7	86.8	84.1
Jul-2019	85.7	88.4	75.3	78.6	85.0	88.2	85.4
Aug-2019	85.7	88.4	75.3	78.6	85.0	88.2	85.4
Sep-2019	81.9	84.5	71.9	75.1	81.2	84.3	81.6
Oct-2019	82.0	84.6	72.0	75.2	81.3	84.4	81.7
Nov-2019	81.1	83.6	71.2	74.4	80.4	83.4	80.8
Dec-2019	82.3	84.9	72.3	75.5	81.6	84.7	82.0
Jan-2020	80.3	83.7	74.8	73.7	83.4	73.3	92.0
Feb-2020	75.9	79.2	70.7	69.6	78.8	69.3	86.9
Mar-2020	60.6	63.2	56.4	55.6	62.9	55.3	69.4
Apr-2020	36.6	38.2	34.1	33.6	38.0	33.4	41.9
May-2020	50.7	52.9	47.2	46.5	52.6	46.3	58.1
Jun-2020	57.6	60.1	53.6	52.8	59.8	52.6	66.0
Jul-2020	57.9	60.4	53.9	53.1	60.1	52.8	66.3
Aug-2020	58.5	61.0	54.5	53.7	60.7	53.4	67.0
Sep-2020	60.1	62.7	56.0	55.1	62.4	54.9	68.8
Oct-2020	60.2	62.8	56.1	55.2	62.5	54.9	69.0
Nov-2020	58.0	60.5	54.0	53.2	60.2	52.9	66.4
Dec-2020	57.5	60.0	53.5	52.7	59.7	52.5	65.9
Jan-2021	54.1	54.6	47.4	41.0	49.9	58.8	61.6
Feb-2021	55.4	55.9	48.5	42.0	51.0	60.2	63.0
Mar-2021	62.3	62.9	54.6	47.2	57.4	67.7	70.9
Apr-2021	63.3	63.9	55.4	48.0	58.3	68.8	72.0
May-2021	65.8	66.4	57.6	49.9	60.6	71.5	74.9
Jun-2021	69.6	70.3	61.0	52.8	64.1	75.6	79.2
Jul-2021	73.1	73.8	64.0	55.4	67.4	79.4	83.2
Aug-2021	70.0	70.7	61.3	53.1	64.5	76.0	79.6
Sep-2021	67.6	68.3	59.2	51.2	62.3	73.4	76.9
Oct-2021	70.6	71.3	61.8	53.5	65.1	76.7	80.3
Nov-2021	71.3	72.0	62.4	54.1	65.7	77.5	81.1
Dec-2021	72.3	73.0	63.3	54.8	66.6	78.5	82.3
Jan-2022	64.5	65.1	56.5	48.9	59.4	70.1	73.4

Table S7: Regional assignment of the passenger load factor for each flight using the origin ICAO airport code. Source: Wikipedia (n.d.).

First Letter of ICAO Airport Code	Description	Assigned Region
A	Western South Pacific	Asia Pacific
B	Greenland, Iceland & Kosovo	Europe
C	Canada	North America
D	Eastern parts of West Africa and Maghreb	Africa
E	Northern Europe	Europe
F	Central Africa, Southern Africa, and Indian Ocean	Africa
G	Western parts of West Africa and Maghreb	Africa
H	East Africa and Northeast Africa	Africa
K	Contiguous United States	North America
L	Southern Europe, Israel, Palestine, and Turkey	Europe
M	Central America, Mexico, and Northern/Western Parts of the Caribbean	Latin America
N	Most of the South Pacific and New Zealand	Asia Pacific
O	Pakistan, Afghanistan, and many West Asian countries	Middle East
P	Most of the North Pacific and Kiribati	Asia Pacific
R	Western part of the North Pacific	Asia Pacific
S	South America	Latin America
T	Eastern and southern parts of the Caribbean	Latin America
U	Most former Soviet countries	Asia Pacific
V	Many South Asian countries, mainland Southeast Asia, Hong Kong, and Macau	Asia Pacific
W	Most of Maritime Southeast Asia	Asia Pacific
Y	Australia	Asia Pacific
Z	China, North Korea, and Mongolia	Asia Pacific

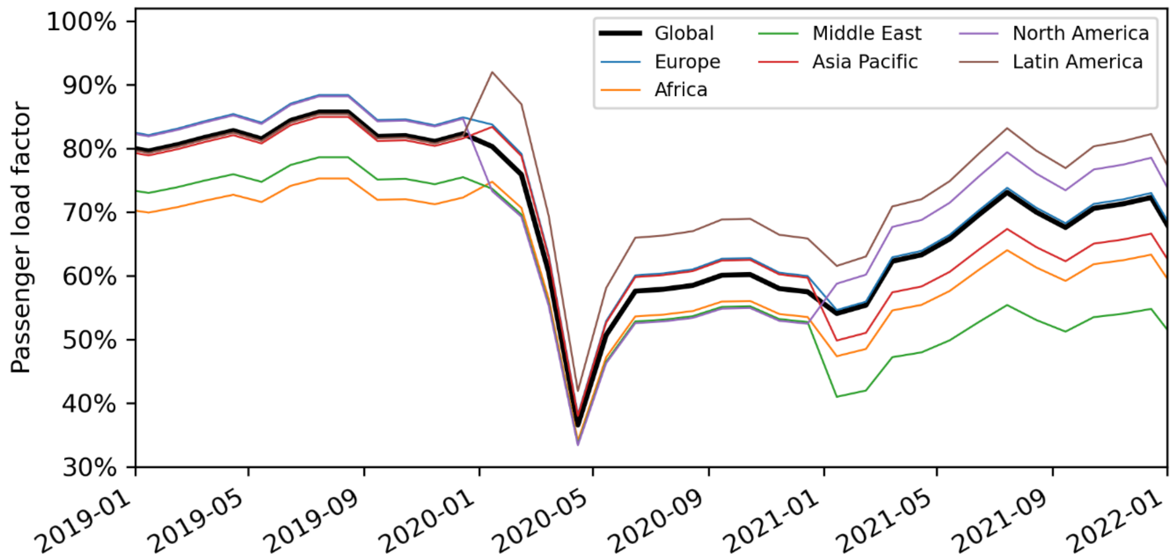

Figure S10: Global and regional passenger load factor between 2019 to 2021 assumed in this study.

S4 nvPM emissions

The three methods used in this study to estimate the nvPM number emissions index (EI_n) and mass emissions index (EI_m) are listed in order of priority:

i. for aircraft-engine types with nvPM measurements available in the ICAO EDB (EASA, 2021), the nvPM EI_n and EI_m are estimated using the T_4/T_2 methodology (Teoh et al., 2022a, b),

ii. for aircraft-engine types where nvPM measurements is not available in the ICAO EDB, the nvPM is estimated according to the methodology of Teoh et al. (2020), where the nvPM EI_m is estimated by using the average value of the Formation and Oxidation (FOX) (Stettler et al., 2013) and Improved FOX (ImFOX) methods (Abrahamson et al., 2016), both of which assumes the emissions profile of single annular combustors, and the nvPM EI_n is estimated from the EI_m using the fractal aggregates (FA) model (Teoh et al., 2019, 2020), and

iii. for remaining aircraft types where engine-specific data is not available, the nvPM EI_m and EI_n are assumed to be 0.088 g kg^{-1} and 10^{15} kg^{-1} respectively (Stettler et al., 2013; Schumann et al., 2015; Teoh et al., 2020).

We describe the T_4/T_2 methodology in detail in Section S4.1 and summarise the FA model in Section S4.2.

S4.1 T_4/T_2 methodology

The T_4/T_2 methodology was originally developed by Teoh et al. (2022a) to estimate the cruise nvPM based on measurements provided by the ICAO EDB. In particular, the nvPM emissions profile for all in-production and new turbofan engines with rated thrust > 26.7 kN (~178 unique engines) are constructed using the four ICAO certification test points, and the nvPM emissions at cruise are estimated by linear interpolation relative to the ratio of turbine-inlet (T_4) to compressor-inlet temperature (T_2), a non-dimensional measure of engine thrust settings (Cumpsty and Heyes, 2015).

Here, we update the T_4/T_2 methodology with two improvements: (i) an improved estimate of T_4 that is informed using data from the ECLIF II/ND-MAX experimental campaign (Schripp et al., 2022; Bräuer et al., 2021; Voigt et al., 2021), where ground and cruise nvPM EI_n were measured behind an Airbus A320 powered by two IAE V2527-A5 engines; and (ii) an incorporation of the step change in nvPM emission profile for staged combustors such as the double annular combustor (DAC) and the twin annular premixing swirler (TAPS) engine (Boies et al., 2015; Stickles and Barrett, 2013).

Fig. S11 summarises the thermodynamic equations used to calculate T_4/T_2 for each waypoint, and the changes applied to improve the T_4/T_2 methodology are highlighted in red. Detailed description of these thermodynamic equations can be found in the Supporting Information §S2.2 of Teoh et al. (2022a). In the original study (Teoh et al., 2022a), the engine thrust settings ($\frac{F}{F_{00,\mathrm{max}}}$) was estimated by dividing the fuel mass flow rate at cruise conditions ($\dot{m}_{\mathrm{f}}^{\mathrm{Cruise}}$) by the maximum fuel mass flow rate ($\dot{m}_{\mathrm{f,max}}$) that is provided by the ICAO EDB,

$$\frac{F}{F_{00,\mathrm{max}}} = \frac{\dot{m}_{\mathrm{f}}^{\mathrm{Cruise}}}{\dot{m}_{\mathrm{f,max}}}. \tag{S4}$$

However, an evaluation of the nvPM EI_n measurements from the ECLIF II/ND-MAX experimental campaign (Schripp et al., 2022; Bräuer et al., 2021; Voigt et al., 2021) suggests that Eq. (S4) could underestimate T_4/T_2 at cruise conditions (Fig. S12a). To address this, we refer to the Fuel Flow Method 2 (FFM2) methodology to convert the $\dot{m}_{\mathrm{f}}^{\mathrm{Cruise}}$ to an equivalent fuel mass flow rate at mean sea level conditions ($\dot{m}_{\mathrm{f}}^{\mathrm{MSL}}$) which is then used to estimate $\frac{F}{F_{00,\mathrm{max}}}$ (DuBois and Paynter, 2006),

$$\frac{F}{F_{00,\mathrm{max}}} = \frac{\dot{m}_{\mathrm{f}}^{\mathrm{MSL}}}{\dot{m}_{\mathrm{f,max}}}. \tag{S5}$$

$$\text{where } \dot{m}_{\mathrm{f}}^{\mathrm{MSL}} = \dot{m}_{\mathrm{f}}^{\mathrm{Cruise}} \left(\frac{T_{\mathrm{amb}}}{T_{\mathrm{MSL}}}\right)^{3.8} \left(\frac{p_{\mathrm{MSL}}}{p_{\mathrm{amb}}}\right) e^{0.2M^2}.$$

Eq. (S5) leads to a 12% increase in T_4/T_2 relative to Eq. (S4), and the cruise nvPM $\mathrm{EI_n}$ measurements are more in-line with the nvPM emissions profile that is provided by the ICAO EDB (Fig. S12b). Future work is currently ongoing to further assess the performance of the T_4/T_2 methodology against: (i) cruise nvPM measurements from more recent experimental campaigns; and (ii) different aircraft-engine combinations.

The nvPM emissions profile varies with different engine combustor type (EASA, 2021), and for most engines, the nvPM $\mathrm{EI_n}$ is continuous across the range of $\frac{F}{F_{00,\mathrm{max}}}$. However, experimental measurements have showed a step change in the nvPM emissions ($\mathrm{EI_n}$ and $\mathrm{EI_m}$) for staged combustors such as the DAC and TAPS engines (Boies et al., 2015; Stickles and Barrett, 2013): at low $\frac{F}{F_{00,\mathrm{max}}}$ (pilot stage), the engine operates in a fuel-rich environment with a low air-to-fuel ratio and the nvPM emissions increases with $\frac{F}{F_{00,\mathrm{max}}}$; and at above an $\frac{F}{F_{00,\mathrm{max}}}$ threshold, the engine operates with a higher air-to-fuel ratio (lean combustion stage) and the nvPM emissions experiences a step change, where the nvPM $\mathrm{EI_n}$ and $\mathrm{EI_m}$ is lower by up to four orders of magnitude when compared with the pilot stage. The DAC combustor is primarily used in the Boeing 777 aircraft (GE90 engine family), while the TAPS combustor (CFM LEAP and GEnx engines) powers the Boeing 737 MAX, a subset of Airbus A320neo and the Boeing 787 Dreamliner (refer to Table S3). To construct the nvPM emissions profile for these staged combustors, we utilize the four ICAO certification test points (7%, 30%, 85% and 100% $\frac{F}{F_{00,\mathrm{max}}}$) that is provided by the ICAO EDB (EASA, 2021): a linear interpolation of the nvPM emissions is used when $\frac{F}{F_{00,\text{max}}}$ is between 7% and 30%; and above 30% $\frac{F}{F_{00,\text{max}}}$, we assume that the engine operates in the lean combustion mode where the nvPM emissions stays constant with the average EI_n and EI_m value at 85% and 100% $\frac{F}{F_{00,\text{max}}}$.

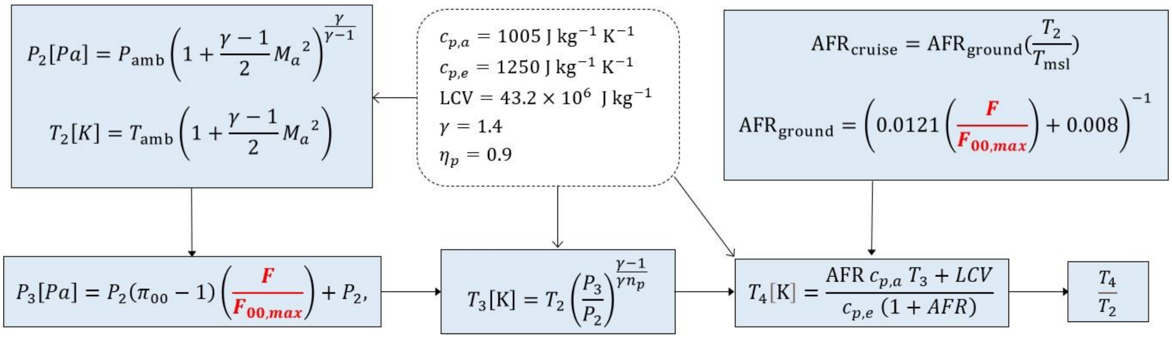

Figure S11: Thermodynamic equations that is used to calculate the non-dimensional engine thrust settings (T_4/T_2). The engine thrust settings ($\frac{F}{F_{00,max}}$), highlighted in red, is updated in this study and calculated using Eq. (S5) to improve the T_4/T_2 methodology. Detailed descriptions of these equations can be found in the Supporting Information §S2.2 of Teoh et al. (2022a).

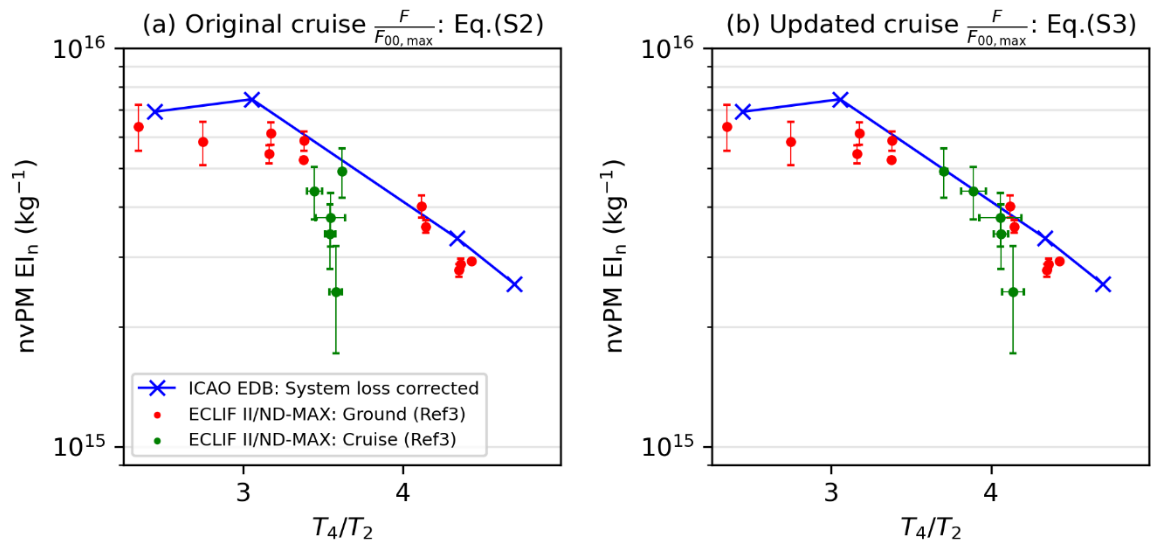

Figure S12: Comparison of the ground (in red) and cruise nvPM EI_n (in green) measured behind an Airbus A320 (powered by two IAE V2527-A5 engines) during the ECLIF II/ND-MAX campaign relative to the four nvPM certification data points provided by the ICAO EDB (in blue), where the non-dimensional engine thrust settings (T_4/T_2) at cruise is calculated using: (a) the original approach outlined in Eq. (S4); and (b) the updated approach outlined in Eq. (S5).

S4.2 Fractal aggregates model

The nvPM emissions profile for older aircraft-engine types is not provided by the ICAO EDB (EASA, 2021) and previous studies used the fractal aggregates (FA) model to estimate the nvPM EI_n for these subset of flights (Teoh et al., 2019, 2020, 2022a, b). The FA model converts the estimated nvPM EI_m to EI_n with assumptions on the nvPM particle size distribution and morphology (Teoh et al., 2020, 2019),

$$\mathrm{EI_n} = \frac{\mathrm{EI_m}}{\rho_0 (\frac{\pi}{6}) (k_{\mathrm{TEM}})^{3-D_{\mathrm{fm}}} \mathrm{GMD}^{\varphi} \exp{(\frac{\varphi^2 \ln(\mathrm{GSD})^2}{2})}} \tag{S6}$$

where $\varphi = 3D_{\mathrm{TEM}} + (1 - D_{\mathrm{TEM}})D_{\mathrm{fm}}$.

The nvPM EI_m is estimated by taking the average of the outputs provided by the FOX (Stettler et al., 2013) and ImFOX methods (Abrahamson et al., 2016). GMD is the geometric mean diameter and is estimated as a function of T_4/T_2 (Teoh et al., 2020),

$$\mathrm{GMD[nm]} = 2.5883 \left(\frac{T_4}{T_2}\right)^2 - 5.3723 \left(\frac{T_4}{T_2}\right) + 16.721 + \delta_{\mathrm{loss}}, \tag{S7}$$

where δ_{loss} is a correction factor that accounts for particle losses at the instrument sampling point and is set to a nominal value of -5.75 nm (Teoh et al., 2020). GSD is the geometric standard deviation (assumed to be 1.80) (Teoh et al., 2020), ρ_0 is the black carbon material density (1770 kg m^{-3}) (Park et al., 2004), D_{fm} is the mass-mobility exponent of black carbon aggregates (2.76), and k_{TEM} (1.621×10^{-5}) and D_{TEM} (0.39) are the transmission electron microscopy prefactor and exponent coefficients respectively (Dastanpour and Rogak, 2014).

S5 Global aviation emissions inventory

S5.1 Annual statistics: 2019 - 2021

The global aviation emissions inventory for 2019–2021 is named as the Global Aviation Emissions Inventory based on ADS-B (GAIA). Fig. S13 shows the distribution of the 2019–2021 annual fuel consumption by longitude, latitude, and altitude, where ~92% of the 2019 annual fuel consumption occurred in the Northern Hemisphere. Fig. 3b in the main text shows that the mean nvPM EI_m and EI_n above 45,000 feet (0.39 g kg^{-1} and 4.5 $\times 10^{15}$ kg^{-1}) are around 4–5 times larger than the global mean values (0.076 g kg^{-1} and 1.0 $\times 10^{15}$ kg^{-1}) because of a higher prevalence of private business jets whose mean nvPM EI_m and EI_n can be up to 0.58 g kg^{-1} and 7 $\times 10^{15}$ kg^{-1} respectively (Table S8). Tables S9 and S10 break down the 2020 and 2021 global aviation activity, fuel consumption, and emissions into 11 key regions. In 2019, the mean fuel consumption per flight distance in China (4.99 kg km^{-1}) is 52% and 21% larger than the US (3.29 kg km^{-1}) and Europe (4.14 kg km^{-1}) respectively (Table 4 in the main text), and this could be due to the: (i) higher proportion of flights cruising at lower altitudes of between 25,000 and 35,000 feet (44% of the total flight distance flown) when compared to other regions (31% of the flight distance flown globally) (Fig. S14); and (ii) differences in the fleet composition mix (proportion of narrow-body-to-wide-body aircraft) in different regions.

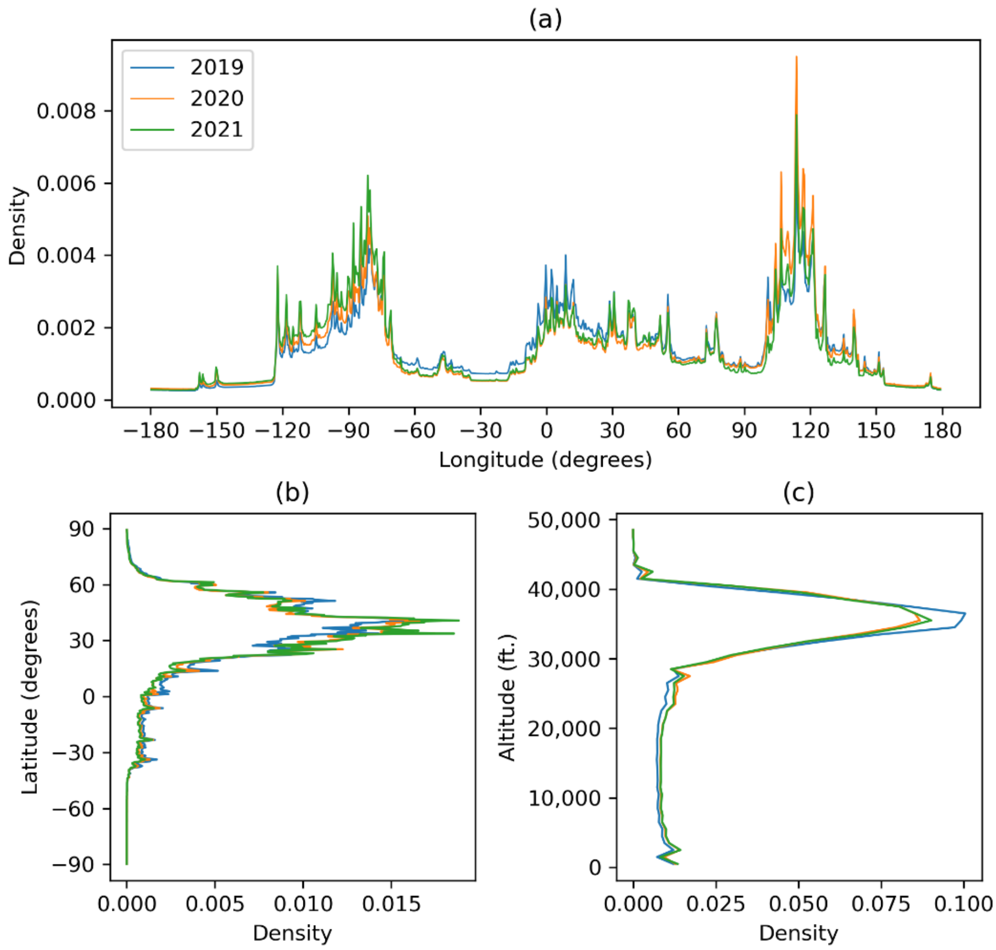

Figure S13: Probability density function of the annual fuel consumption from GAIA by: (a) longitude; (b) latitude; and (c) altitude for 2019 (in blue), 2020 (in orange) and 2021 (in green).

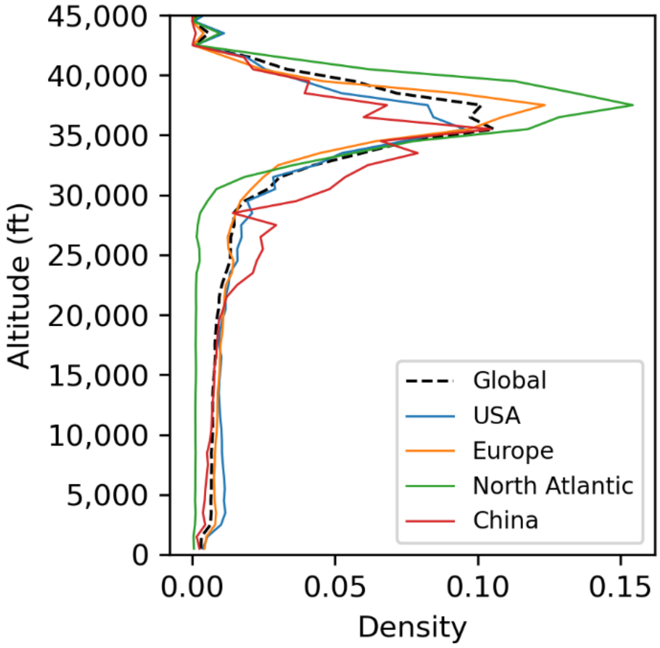

Figure S14: Probability density function of the 2019 annual flight distance flown in GAIA by altitude across the globe (black dotted line), and over the USA (in blue), Europe (in orange), North Atlantic (in green) and China (in red).

Table S8: Top 10 commonly used aircraft types above 45,000 feet and their mean nvPM EI_n in GAIA.

Aircraft type	% of the total distance flown above 45,000 feet between 2019 and 2021	Mean nvPM EI_n ($\times 10^{15}$ kg^{-1})	Mean nvPM EI_m (g kg^{-1})
GLF5	26.4%	7.14	0.52
GLF6	17.2%	6.81	0.55
C750	16.5%	0.32	0.036
GLEX	14.7%	7.12	0.055
GL5T	4.2%	7.09	0.54
F2TH	3.7%	4.51	0.59
FA7X	3.4%	2.29	0.084
LJ45	2.2%	0.26	0.025
LJ75	1.2%	0.31	0.029
F900	1.1%	0.28	0.028

S5.2 Flight-level statistics

GAIA, which contains 103.7 million unique flight trajectories between 2019 and 2021, is used to provide statistics on the distribution of air traffic activity and emissions by flight mission profile. Table 5 in the main text categorises the 2019 global air traffic activity and emissions into short-, medium-, and long-haul flights based on their duration, while Tables S11 and S12 provide these statistics for 2020 and 2021 respectively. Each flight in 2019 is also grouped by their origin-destination (OD) airport pairs and corresponding countries to evaluate the difference in their mean: (i) historical flight distance flown (d_{GAIA}) versus the great circle trajectory between the origin-destination airport pairs (d_{OD}); and (ii) simulated fuel consumption from the actual flight trajectory in GAIA (f_{GAIA}) versus the estimated fuel consumption at climb, cruise, and descent (CCD) from the great circle trajectory ($f_{\mathrm{EEA,OD}}$) which is derived from an emissions calculator developed by the European Environment Agency using inputs of d_{OD} and aircraft type (European Environment Agency, 2019). These statistics, which vary significantly between OD airport pairs (Fig. 8 in the main text and Fig. S15), have been made publicly available as described in the Data Availability statement (main text). Across all OD airport pairs, we estimate a mean $d_{\mathrm{GAIA}}/d_{\mathrm{OD}}$ of 1.06 [1.01, 1.16] (5th and 95$^{\mathrm{th}}$ percentile) and a mean $f_{\mathrm{GAIA}}/f_{\mathrm{EEA,OD}}$ of 1.14 [0.997, 1.35] (Fig. S15). We also note that the variability of $f_{\mathrm{GAIA}}/f_{\mathrm{EEA,OD}}$ is greater than $d_{\mathrm{GAIA}}/d_{\mathrm{OD}}$, and this can most likely be attributed to the: (i) use of different aircraft types (i.e., narrow- and wide-body aircraft) to complete the same mission; and the day-to-day variability in (ii) passenger load factor (LF); and (iii) ambient wind fields (i.e., headwind and tailwind).

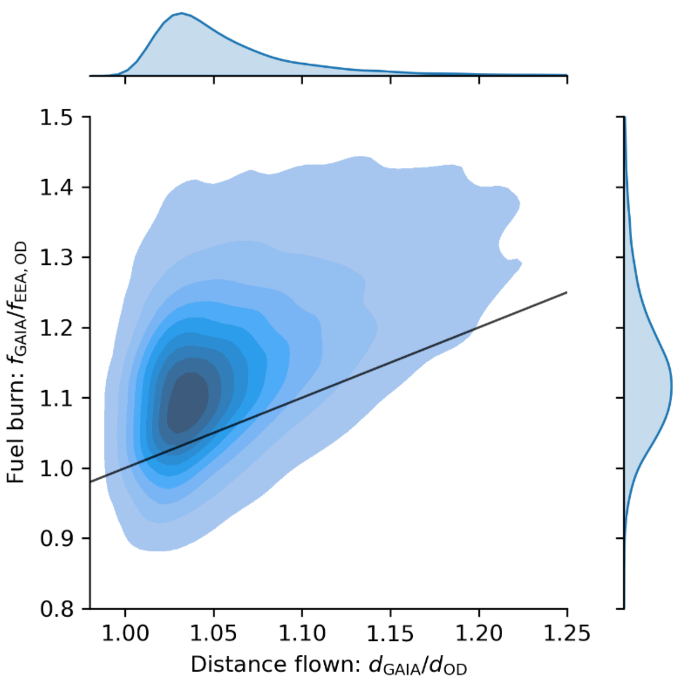

Figure S15: Kernel density estimate between the mean ratios of $f_{\mathrm{GAIA}}/f_{\mathrm{EEA,OD}}$ and $d_{\mathrm{GAIA}}/d_{\mathrm{OD}}$ for each origin-destination airport pairs globally in 2019 (n = 36,626).

Fig. 9 in the main text highlights the variability in flight trajectory, fuel consumption and emissions for eastbound and westbound flights between London Heathrow (LHR) and Singapore Changi Airport (SIN) in 2019-2021, totalling 8,705 unique flights. During this time, the three main aircraft types used for this route are the Boeing 777 (40.8% of all flights), Airbus A380 (38.6%), and the Airbus A350 (20.6%); and the three main airline operators are Singapore Airlines (65.0% of all flights), British Airways (23.9%), and Qantas Airways (8.9%). For each flight, the fuel consumption per passenger-km is calculated as follows:

$$\text{Fuel per passenger-km} = \frac{\text{Total fuel burn}}{(\text{Aircraft seat capacity} \times \text{Passenger LF}) \times \text{Flight distance flown}}, \qquad \text{(S8)}$$

where the registered seat capacity for each unique aircraft is provided by the Cirium global fleet database (Cirium, 2022), while the methodology to estimate the passenger LF is described in SI §S3. We note that the coefficient of variation (CV), i.e., the ratio of the standard deviation to the mean, of the fuel consumption per passenger-km (0.171) is around 8 times larger than the CV of the flight distance flown (0.021), which most likely arises from: (i) the use of different aircraft-engine types; (ii) variabilities in aircraft seating capacity between airlines; as well as the day-to-day variability in the (iii) passenger LF; and (iv) ambient wind conditions.

Table S9: Regional aviation activity, fuel consumption and emissions for 2020.

Regional statistics: 2020	Global	USA	Europe	East Asia	SEA	Latin America	Africa & Middle East	China	India	North Atlantic	North Pacific	Arctic Region
Distance travelled (x10^9 km)	34.50	11.27	3.592	6.298	1.569	1.072	2.015	6.848	1.257	1.159	1.610	0.160
- Percentage by region[a]	-	33%	10%	18%	4.5%	3.1%	5.8%	20%	3.6%	3.4%	4.7%	0.5%
Air traffic density (km^{-1} h^{-1})[b]	0.008	0.080	0.062	0.044	0.012	0.003	0.004	0.036	0.016	0.012	0.008	0.001
Fuel burn (Tg)	146	32.4	14.6	29.5	7.73	4.45	9.91	31.6	6.20	6.83	10.8	1.14
- Percentage by region[a]	-	22%	10%	20%	5.3%	3.0%	6.8%	22%	4.2%	4.7%	7.4%	0.8%
Fuel burn per dist. (kg km^{-1})	4.240	2.875	4.065	4.684	4.927	4.151	4.918	4.614	4.932	5.893	6.714	7.125
CO_2 (Tg)	462	102	46.1	93.2	24.4	14.1	31.3	100	19.6	21.6	34.1	3.60
H_2O (Tg)	180	39.9	18.0	36.3	9.51	5.47	12.2	38.9	7.63	8.40	13.3	1.40
OC (Gg)	2.93	0.648	0.292	0.590	0.155	0.089	0.198	0.632	0.124	0.137	0.216	0.023
SO_2 (Gg)	176	38.9	17.5	35.4	9.28	5.34	11.9	37.9	7.44	8.20	13.0	1.37
S^{VI} (Gg)	3.58	0.793	0.358	0.722	0.189	0.109	0.243	0.774	0.152	0.167	0.265	0.028
NO_X (as NO_2, Tg)	2.26	0.441	0.222	0.456	0.130	0.070	0.160	0.483	0.103	0.108	0.183	0.020
- Percentage by region [a]	-	20%	10%	20%	5.8%	3.1%	7.1%	21%	4.6%	4.8%	8.1%	0.9%
CO (Gg)	227	72.0	30.2	46.3	12.5	6.82	13.0	47.5	7.73	4.07	10.1	0.561
- Percentage by region [a]	-	32%	13%	20%	5.5%	3.0%	5.7%	21%	3.4%	1.8%	4.4%	0.2%
HC (Gg)	20.9	7.55	2.50	3.46	0.95	0.53	1.21	3.52	0.59	0.51	1.03	0.066
- Percentage by region [a]	-	36%	12%	17%	4.5%	2.5%	5.8%	17%	2.8%	2.4%	4.9%	0.3%
nvPM mass (Gg)	9.93	2.86	1.06	2.13	0.540	0.310	0.600	2.25	0.363	0.325	0.452	0.036
- Percentage by region [a]	-	29%	11%	21%	5.4%	3.1%	6.0%	23%	3.7%	3.3%	4.6%	0.4%
nvPM number (x10^{26})	1.464	0.430	0.158	0.335	0.071	0.042	0.080	0.363	0.063	0.039	0.070	0.005
- Percentage by region [a]	-	29%	11%	23%	4.8%	2.9%	5.5%	25%	4.3%	2.7%	4.8%	0.3%
Mean EI NO_X (g kg^{-1})	15.4	13.6	15.2	15.5	16.8	15.7	16.1	15.3	16.6	15.8	16.9	17.4
Mean EI CO (g kg^{-1})	1.55	2.22	2.07	1.57	1.62	1.53	1.31	1.50	1.25	0.60	0.93	0.49
Mean EI HC (g kg^{-1})	0.143	0.233	0.171	0.117	0.123	0.119	0.122	0.112	0.095	0.074	0.096	0.058
Mean nvPM EI_m (g kg^{-1})	0.068	0.088	0.073	0.072	0.070	0.070	0.061	0.071	0.059	0.048	0.042	0.032
Mean nvPM EI_n (x10^{15} kg^{-1})	0.998	1.328	1.085	1.136	0.913	0.954	0.810	1.149	1.010	0.569	0.646	0.413

[a]: The percentages of each region do not add up to 100% because there are some overlapping between the regional bounding boxes; and when taken together, these regions do not cover 100% of Earth's surface area (refer to Fig. 1 and Table 2 in the main text).

[b]: The air traffic density (ATD) is defined as the total flight distance flown in the region divided by its surface area and time, ATD $[\mathrm{km}^{-1}\ \mathrm{h}^{-1}] = \frac{\sum \text{Annual flight distance flown [km]}}{\text{Surface area [km}^2] \times (365\times 24\ [\mathrm{h}])}$.

Table S10: Regional aviation activity, fuel consumption and emissions for 2021.

Regional statistics: 2021	Global	USA	Europe	East Asia	SEA	Latin America	Africa & Middle East	China	India	North Atlantic	North Pacific	Arctic Region
Distance travelled ($x10^9$ km)	41.90	15.17	4.475	5.948	1.208	1.479	2.795	6.654	1.438	1.441	1.736	0.193
- Percentage by region[a]	-	36%	11%	14%	2.9%	3.5%	6.7%	16%	3.4%	3.4%	4.1%	0.5%
Air traffic density (km^{-1} h^{-1})[b]	0.009	0.108	0.077	0.042	0.009	0.004	0.005	0.035	0.018	0.014	0.008	0.001
Fuel burn (Tg)	166	42.5	16.8	27.8	6.14	5.64	12.59	30.2	6.39	8.35	11.5	1.33
- Percentage by region[a]	-	26%	10%	17%	3.7%	3.4%	7.6%	18%	3.9%	5.0%	6.9%	0.8%
Fuel burn per dist. (kg km^{-1})	3.958	2.802	3.761	4.670	5.084	3.811	4.504	4.540	4.440	5.795	6.607	6.909
CO_2 (Tg)	524	134	53.2	87.8	19.4	17.8	39.8	95.4	20.2	26.4	36.2	4.21
H_2O (Tg)	204	52.3	20.7	34.2	7.55	6.93	15.5	37.2	7.85	10.27	14.1	1.64
OC (Gg)	3.32	0.850	0.337	0.556	0.123	0.113	0.252	0.604	0.128	0.167	0.229	0.027
SO_2 (Gg)	199	51.0	20.2	33.3	7.37	6.76	15.1	36.3	7.66	10.02	13.8	1.60
S^{VI} (Gg)	4.06	1.04	0.412	0.680	0.150	0.138	0.308	0.740	0.156	0.204	0.281	0.033
NO_X (as NO_2, Tg)	2.55	0.589	0.253	0.433	0.105	0.087	0.202	0.463	0.104	0.136	0.195	0.024
- Percentage by region[a]	-	23%	10%	17%	4.1%	3.4%	7.9%	18%	4.1%	5.3%	7.7%	0.9%
CO (Gg)	272	93.2	36.4	47.4	10.2	9.56	18.3	49.6	8.99	5.07	11.2	0.703
- Percentage by region[a]	-	34%	13%	17%	3.8%	3.5%	6.7%	18%	3.3%	1.9%	4.1%	0.3%
HC (Gg)	25.0	9.88	2.99	3.47	0.82	0.72	1.60	3.59	0.63	0.58	1.15	0.081
- Percentage by region[a]	-	40%	12%	14%	3.3%	2.9%	6.4%	14%	2.5%	2.3%	4.6%	0.3%
nvPM mass (Gg)	11.0	3.73	1.15	1.84	0.369	0.382	0.731	1.99	0.321	0.389	0.430	0.038
- Percentage by region[a]	-	34%	10%	17%	3.4%	3.5%	6.7%	18%	2.9%	3.5%	3.9%	0.3%
nvPM number ($x10^{26}$)	1.663	0.560	0.179	0.302	0.048	0.054	0.103	0.337	0.065	0.045	0.069	0.005
- Percentage by region[a]	-	34%	11%	18%	2.9%	3.2%	6.2%	20%	3.9%	2.7%	4.2%	0.3%
Mean EI NO_X (g kg^{-1})	15.4	13.9	15.0	15.6	17.2	15.5	16.0	15.3	16.3	16.3	17.0	18.0
Mean EI CO (g kg^{-1})	1.64	2.19	2.16	1.71	1.66	1.70	1.45	1.64	1.41	0.61	0.98	0.53
Mean EI HC (g kg^{-1})	0.151	0.232	0.178	0.125	0.133	0.127	0.127	0.119	0.099	0.070	0.100	0.060
Mean nvPM EI_m (g kg^{-1})	0.066	0.088	0.068	0.066	0.060	0.068	0.058	0.066	0.050	0.047	0.037	0.029
Mean nvPM EI_n ($x10^{15}$ kg^{-1})	1.001	1.317	1.061	1.088	0.774	0.950	0.817	1.116	1.024	0.540	0.604	0.381

[a]: The percentages of each region do not add up to 100% because there are some overlapping between the regional bounding boxes; and when taken together, these regions do not cover 100% of Earth's surface area (refer to Fig. 1 and Table 2 in the main text).

[b]: The air traffic density (ATD) is defined as the total flight distance flown in the region divided by its surface area and time, $\text{ATD}\ [\text{km}^{-1}\ \text{h}^{-1}] = \frac{\sum \text{Annual flight distance flown [km]}}{\text{Surface area [km}^2\text{]} \times (365\times 24\ \text{[h]})}$.

Table S11: Breakdown of aviation activity, fuel consumption and emissions for 2020 by flight duration.

Flight-level statistics: 2020	All flights	Short-haul ($t \leq$ 3h)		Medium-haul ($3 < t \leq 6$)		Long-haul ($t > 6$)	
		Value	% total	Value	% total	Value	% total
Number of flights	27,911,214	24,415,965	87.5%	2,563,329	9.2%	931,920	3.3%
Number of night flights[a]	4,375,917	3,707,150	84.7%	507,657	11.6%	161,110	3.7%
Distance travelled (x10^9 km)	34.50	19.47	56.4%	7.737	22.4%	7.292	21.1%
Fuel burn (Tg)	146	60.4	41.3%	31.2	21.3%	54.7	37.4%
Fuel burn per dist. (kg km^{-1})	4.241	3.102	-	4.035	-	7.499	-
Mean flight time (h)	1.76	1.27	-	3.95	-	9.08	-
Mean flight length (km)	1236	797	-	3018	-	7825	-
Mean aircraft mass (kg)	49593	39896	-	86607	-	211559	-
- Fuel fraction[b]	7.20%	5.69%	-	15.2%	-	26.0%	-
CO_2 (Tg)	462	191	41.3%	99	21.3%	173	37.4%
NO_X (as NO_2, Tg)	2.26	0.829	36.7%	0.447	19.8%	0.983	43.5%
CO (Gg)	227	147	64.8%	40.4	17.8%	39.4	17.4%
HC (Gg)	20.9	12.3	58.9%	4.19	20.0%	4.40	21.1%
nvPM mass (Gg)	9.93	5.35	53.9%	2.38	24.0%	2.20	22.2%
nvPM number (x10^{26})	1.46	0.864	59.2%	0.353	24.2%	0.247	16.9%
Mean EI NO_X (g kg^{-1})	15.45	13.73	-	14.32	-	17.98	-
Mean EI CO (g kg^{-1})	1.55	2.43	-	1.29	-	0.72	-
Mean EI HC (g kg^{-1})	0.14	0.20	-	0.13	-	0.08	-
Mean nvPM EI_m (g kg^{-1})	0.068	0.089	-	0.076	-	0.040	-
Mean nvPM EI_n (x10^{15} kg^{-1})	0.998	1.430	-	1.131	-	0.452	-

[a]: Night flights are identified when their mean solar direct radiation (SDR) throughout their flight trajectory is < 1 W m^{-2}.
[b]: Fuel fraction is the total fuel mass divided by the initial aircraft mass.

Table S12: Breakdown of aviation activity, fuel consumption and emissions for 2021 by flight duration.

Flight-level statistics: 2021	All flights	Short-haul ($t \leq$ 3h)		Medium-haul ($3 < t \leq 6$)		Long-haul ($t > 6$)	
		Value	% total	Value	% total	Value	% total
Number of flights	35,576,376	31,277,810	87.9%	3,278,356	9.2%	1,020,210	2.9%
Number of night flights[a]	4,847,915	4,120,217	85.0%	568,596	11.7%	159,102	3.3%
Distance travelled (x10^9 km)	41.90	24.06	57.4%	9.853	23.5%	7.994	19.1%
Fuel burn (Tg)	166	70.2	42.4%	37.8	22.8%	57.8	34.8%
Fuel burn per dist. (kg km^{-1})	3.957	2.919	-	3.837	-	7.227	-
Mean flight time (h)	1.74	1.26	-	3.95	-	9.06	-
Mean flight length (km)	1178	769	-	3005	-	7836	-
Mean aircraft mass (kg)	46533	37440	-	82687	-	207952	-
- Fuel fraction[b]	6.98%	5.53%	-	14.9%	-	25.6%	-
CO_2 (Tg)	524	222	42.4%	119	22.8%	182	34.8%
NO_X (as NO_2, Tg)	2.55	0.97	37.8%	0.542	21.3%	1.04	40.8%
CO (Gg)	272	179	65.8%	49.9	18.3%	42.7	15.7%
HC (Gg)	25.0	15.2	60.8%	5.26	21.0%	4.56	18.2%
nvPM mass (Gg)	11.0	5.98	54.5%	2.79	25.4%	2.21	20.1%
nvPM number (x10^{26})	1.66	0.984	59.3%	0.427	25.7%	0.252	15.2%
Mean EI NO_X (g kg^{-1})	15.38	13.74	-	14.33	-	18.00	-
Mean EI CO (g kg^{-1})	1.64	2.55	-	1.32	-	0.74	-
Mean EI HC (g kg^{-1})	0.15	0.22	-	0.14	-	0.08	-
Mean nvPM EI_m (g kg^{-1})	0.066	0.085	-	0.074	-	0.038	-
Mean nvPM EI_n (x10^{15} kg^{-1})	1.001	1.401	-	1.129	-	0.436	-

[a]: Night flights are identified when their mean solar direct radiation (SDR) throughout their flight trajectory is < 1 W m^{-2}.
[b]: Fuel fraction is the total fuel mass divided by the initial aircraft mass.

S6 Comparison with other studies

Table S13 compares the 2019–2020 annual fuel consumption, emissions, and mean EI's from GAIA relative to those derived from Quadros et al. (2022). The 2019 annual fuel consumption from GAIA (283 Tg) is 4.7% lower than Quadros et al. (2022) (297 Tg). Fig. S16 compares the spatial distribution of the 2019 annual fuel consumption between our study and Quadros et al. (2022): the fuel consumption from Quadros et al. (2022) are more concentrated along established flight corridors because monthly-averaged flight trajectories were used; while GAIA uses the actual flight trajectories flown which causes the fuel consumption to be more spatially dispersed.

Table S13: Comparison of the 2019–2020 annual fuel consumption, emissions and mean EI's derived from GAIA versus those from Quadros et al. (2022) using Flightradar24 data.

Annual statistics	GAIA		Quadros et al. (2022)		% difference	
	2019	2020	2019	2020	2019	2020
Fuel burn (Tg)	283	146	297	157	-4.7%	-6.9%
CO_2 (Tg)	893	462	937	496	-4.7%	-6.9%
H_2O (Tg)	348	180	367	194	-5.2%	-7.0%
NO_X (Tg)	4.49	2.26	4.62	2.44	-2.8%	-7.4%
CO (Gg)	400	227	814	569	-51%	-60%
HC (Gg)	33.9	20.9	42.6	27.3	-20%	-23%
nvPM mass (Gg)	21.4	9.93	9.68	4.79	121%	107%
nvPM number ($\times10^{26}$)	2.83	1.46	3.47	1.73	-18%	-16%
Mean EI NO_X (g kg^{-1})	15.9	15.4	15.6	15.5	2.2%	-0.6%
Mean EI CO (g kg^{-1})	1.42	1.55	2.74	3.62	-48%	-57%
Mean EI HC (g kg^{-1})	0.120	0.143	0.143	0.174	-16%	-18%
Mean nvPM EI_m (g kg^{-1})	0.076	0.068	0.033	0.031	132%	122%
Mean nvPM EI_n ($\times10^{15}$ kg^{-1})	1.00	1.00	1.17	1.10	-14.3%	-9.4%

Differences in the 2019 mean EI's from different pollutants are between -48% and +132%. In particular, GAIA estimates a lower EI CO (1.4 g kg^{-1}) and HC (0.12 g kg^{-1}) when compared to Quadros et al. (2022) (2.7 g kg^{-1} for CO and 0.14 g kg^{-1} for HC), and these discrepancies could be caused by the exclusion of ground emissions in GAIA where the EI's of these pollutants are generally at a maximum during the taxi phase (Fig. S19 and S20). Fig. S17 breaks down the fuel consumption and mean EI's from the two studies by altitude. At cruise altitudes (between 30,000 and 40,000 feet), large differences are observed in the total fuel consumption because

Quadros et al. (2022) assumed a constant cruise altitude for each aircraft type in the modelled flight trajectory. There are also large discrepancies in the EI's of CO, HC and nvPM EI_n specifically at altitudes below 10,000 feet and above 30,000 feet, and these likely arise from the treatment of aircraft-engine assignments between both studies. Aircraft-engine assignments in GAIA uses a global fleet database (Cirium, 2022) whenever possible to obtain the specific aircraft variant and engine model (covering 59% of all flights or 79% of flights by jet aircraft, SI §S2), while Quadros et al. (2022) compiled data on the aircraft-type-specific engine market share and aggregated the global emissions with a weighted average of their respective market share. Fig. S18 to S22 illustrates the variations in the emissions profile of NO_X, CO, HC, and nvPM for different aircraft-engine combinations, where specific aircraft types such as the Airbus A320, A20N, and Boeing 787 have large variations among the different engine options available. Fig. S17f also shows that the difference in nvPM EI_m from both studies generally increases with altitude, and this could be due to use of the Döpelheuer & Lecht relation (Peck et al., 2013; Döpelheuer and Lecht, 1998) in Quadros et al. (2022) to scale nvPM emissions from ground to cruise which could underestimate the nvPM EI_m (Abrahamson et al., 2016).

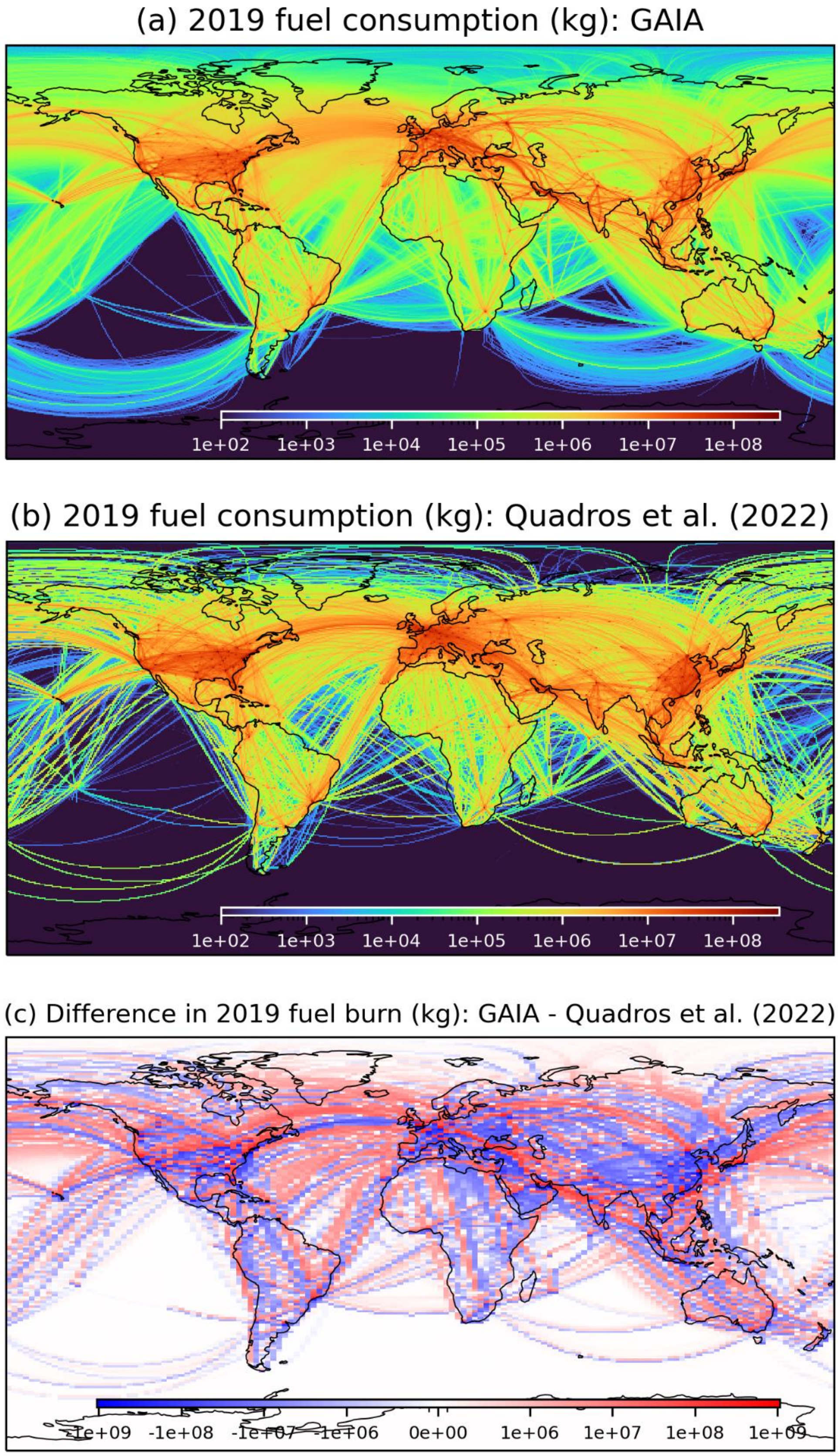

Figure S16: Spatial distribution of the 2019 annual fuel consumption from (a) GAIA with actual flight trajectories versus (b) estimates from Quadros et al. (2022) which used monthly-averaged flight trajectories, and (c) the absolute difference in annual fuel consumption between (a) and (b). Basemap plotted using Cartopy 0.21.1 © Natural Earth; license: public domain.

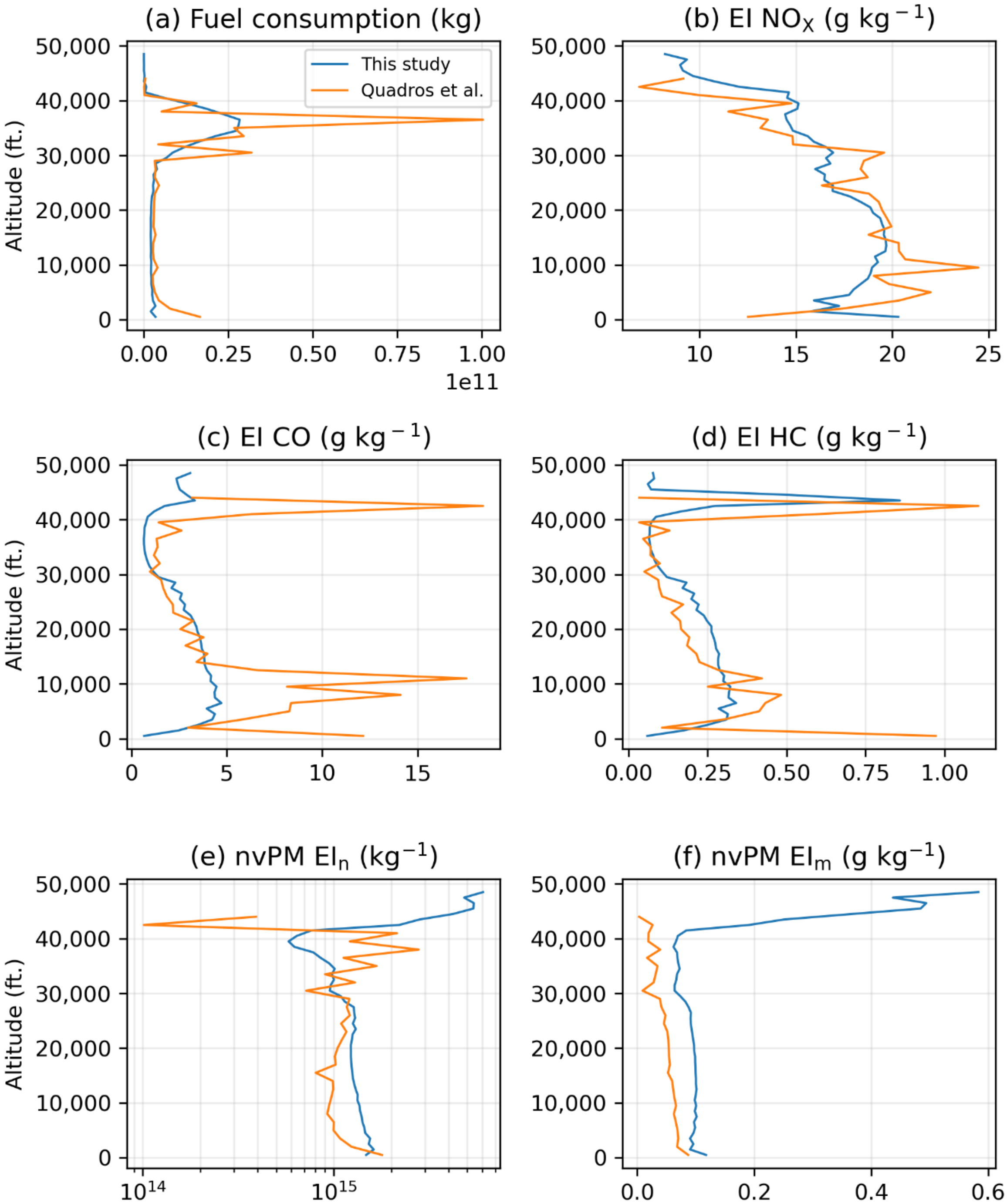

Figure S17: Breakdown of the 2019 annual: (a) fuel consumption, the EI's of (b) NO_X, (c) CO, (d) HC, and the nvPM (e) EI_n and (f) EI_m that is derived from this study (blue lines) versus those from Quadros et al. (2022) (orange lines).

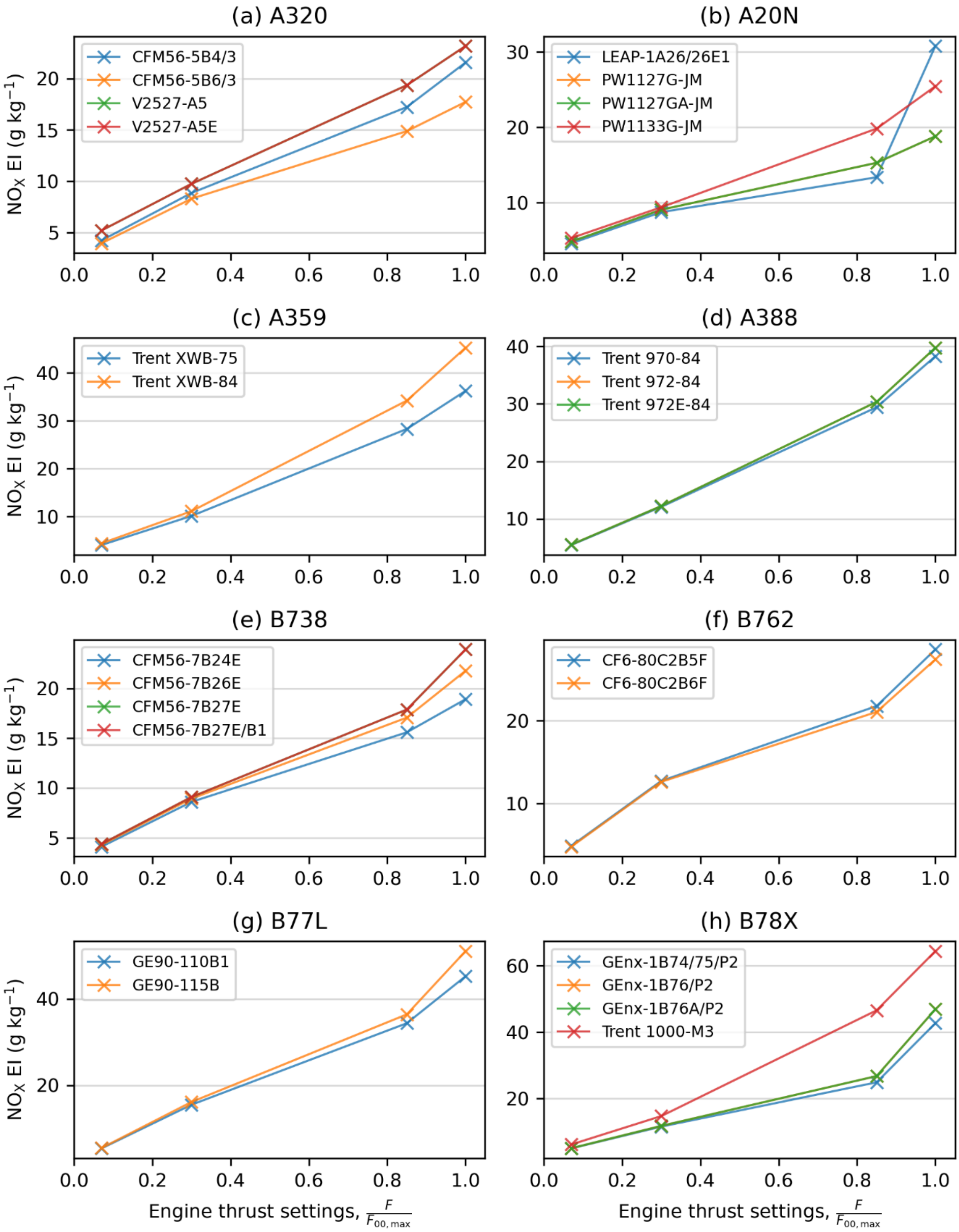

Figure S18: ICAO EDB measurements of the NO_X EI at the four certification test points (7%, 30%, 85% and 100% engine thrust settings) for selected aircraft-engine pairs.

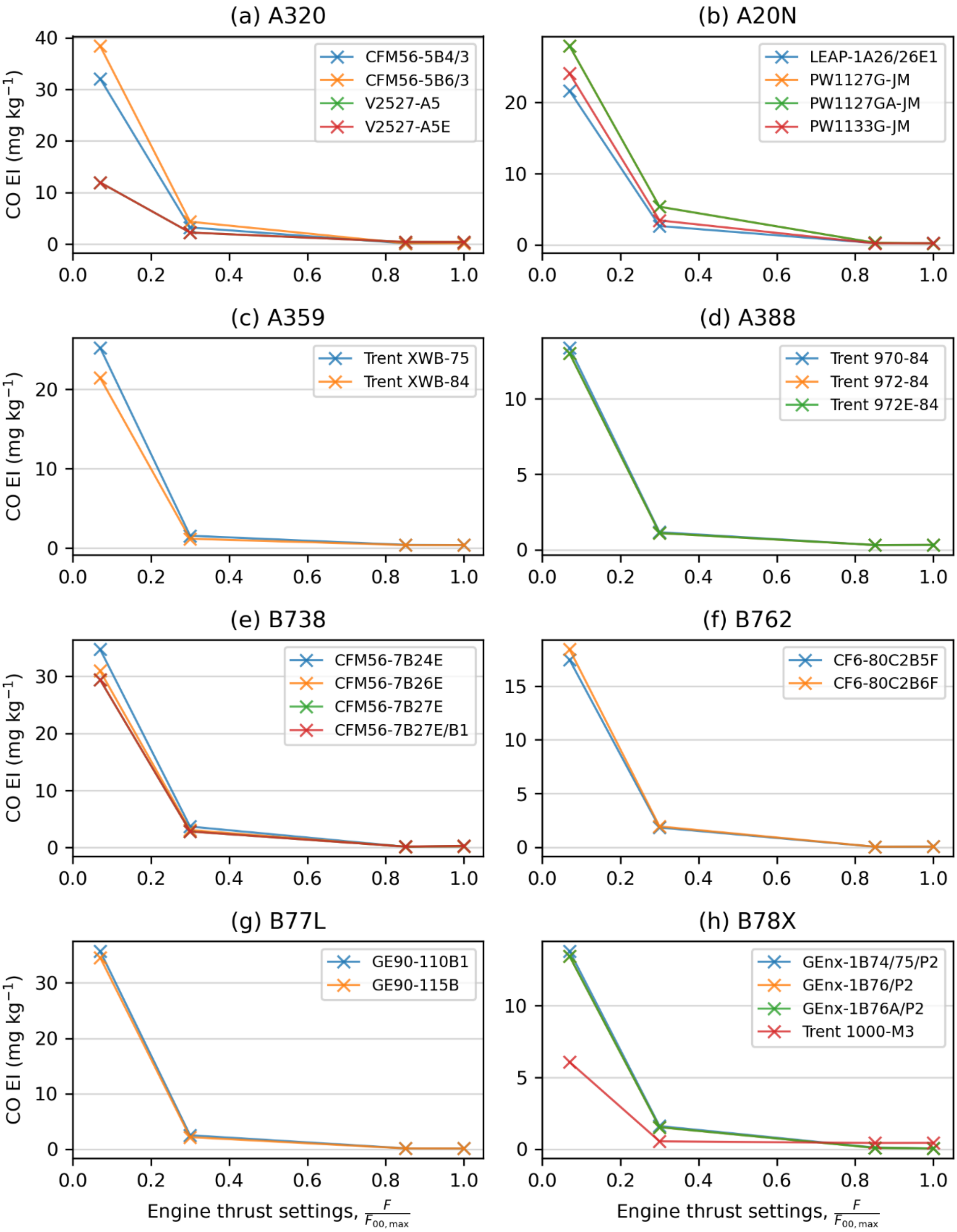

Figure S19: ICAO EDB measurements of the CO EI at the four certification test points (7%, 30%, 85% and 100% engine thrust settings) for selected aircraft-engine pairs.

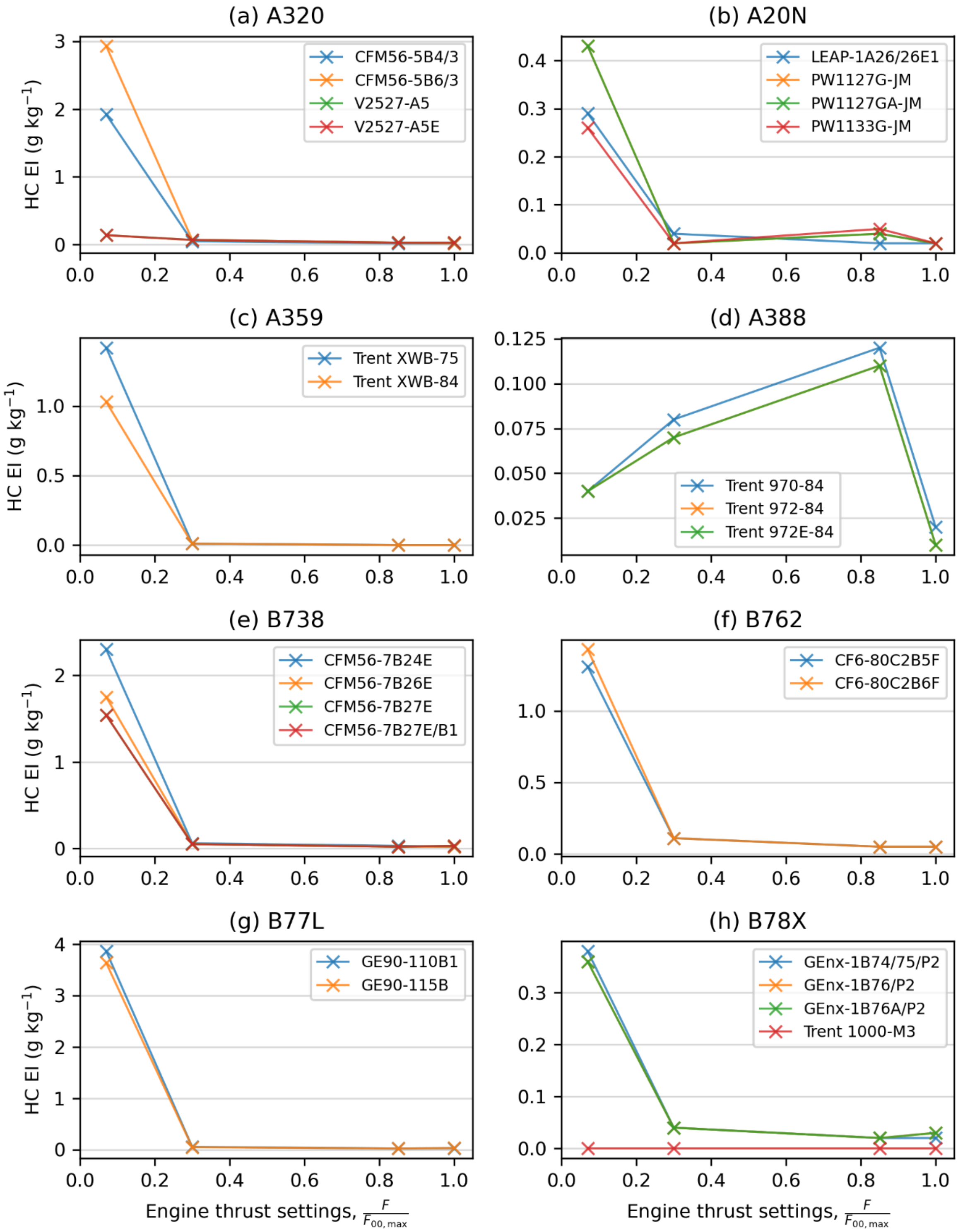

Figure S20: ICAO EDB measurements of the HC EI at the four certification test points (7%, 30%, 85% and 100% engine thrust settings) for selected aircraft-engine pairs.

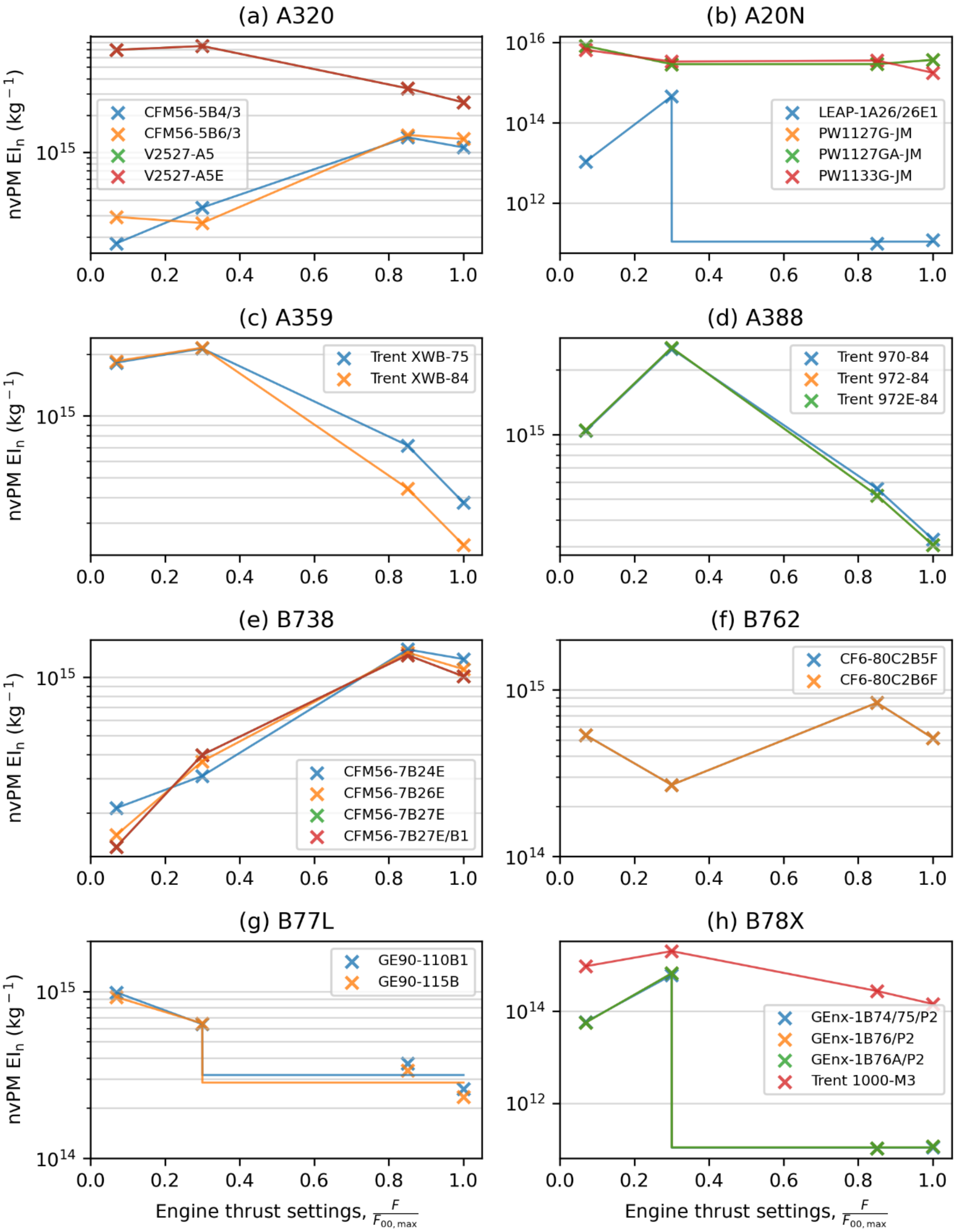

Figure S21: ICAO EDB measurements of the nvPM EI_n that is corrected for particle losses at the four certification test points (7%, 30%, 85% and 100% engine thrust settings) for selected aircraft-engine pairs. The nvPM emissions profile for each engine (individual lines) is constructed using the methodology outlined in the SI §S4, which accounts for the step change in nvPM emissions from staged combustors.

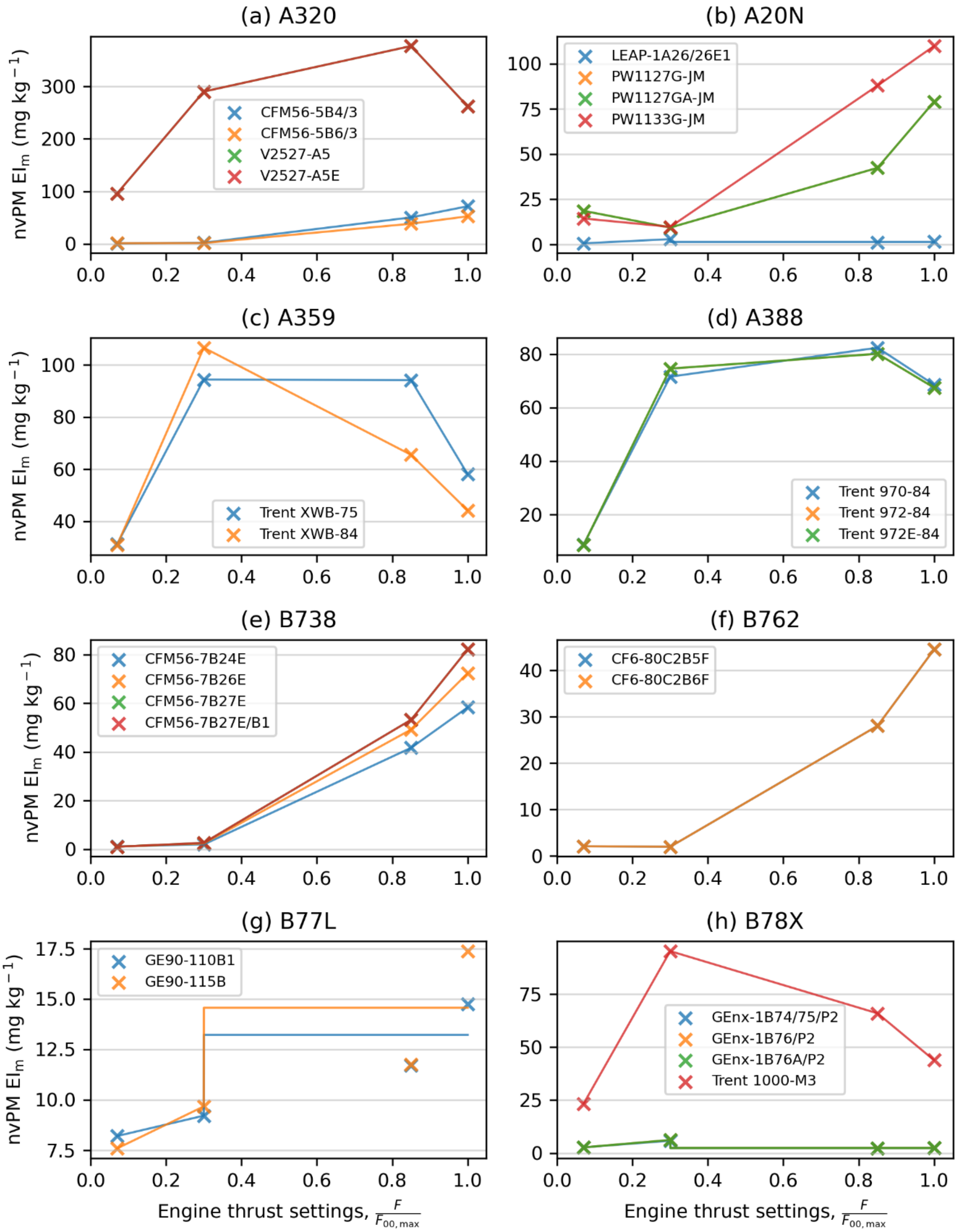

Figure S22: ICAO EDB measurements of the nvPM EI_m that is corrected for particle losses at the four certification test points (7%, 30%, 85% and 100% engine thrust settings) for selected aircraft-engine pairs. The nvPM emissions profile for each engine (individual lines) is constructed using the methodology outlined in the SI §S4, which accounts for the step change in nvPM emissions from staged combustors.

References

Abrahamson, J. P., Zelina, J., Andac, M. G., and Vander Wal, R. L.: Predictive Model Development for Aviation Black Carbon Mass Emissions from Alternative and Conventional Fuels at Ground and Cruise, Environ. Sci. Technol., 50, 12048–12055, https://doi.org/10.1021/acs.est.6b03749, 2016.

Airlines for America: World Airlines Traffic and Capacity, https://www.airlines.org/dataset/world-airlines-traffic-and-capacity/, 2022. Last access: 12 August 2022.

Boies, A. M., Stettler, M. E. J., Swanson, J. J., Johnson, T. J., Olfert, J. S., Johnson, M., Eggersdorfer, M. L., Rindlisbacher, T., Wang, J., and Thomson, K.: Particle emission characteristics of a gas turbine with a double annular combustor, Aerosol Sci. Technol., 49, 842–855, https://doi.org/10.1080/02786826.2015.1078452, 2015.

Bräuer, T., Voigt, C., Sauer, D., Kaufmann, S., Hahn, V., Scheibe, M., Schlager, H., Diskin, G. S., Nowak, J. B., DiGangi, J. P., Huber, F., Moore, R. H., and Anderson, B. E.: Airborne Measurements of Contrail Ice Properties—Dependence on Temperature and Humidity, Geophys. Res. Lett., 48, e2020GL092166, https://doi.org/10.1029/2020GL092166, 2021.

Changi Airport Group: Changi Airport handled 68.3 million passengers in 2019, https://www.changiairport.com/corporate/media-centre/newsroom.html#/pressreleases/changi-airport-handled-68-dot-3-million-passengers-in-2019-2966486, 2020. Last access: 16 August 2022.

Changi Airport Group: Traffic Statistics, https://www.changiairport.com/corporate/our-expertise/air-hub/traffic-statistics.html, 2022. Last access: 16 August 2022a.

Cirium: Aircraft fleets and values: the world's largest independent aircraft database, https://www.cirium.com/solutions/fleets-and-valuations/, 2022. Last access: 30 November 2022.

Cumpsty, N. A. and Heyes, A.: Jet propulsion: A simple guide to the aerodynamics and thermodynamic design and performance of jet engines, Third Edition., Cambridge University Press, 2015.

Dalmau, R. and Prats, X.: Assessing the impact of relaxing cruise operations with a reduction of the minimum rate of climb and/or step climb heights, Aerosp. Sci. Technol., 70, 461–470, https://doi.org/10.1016/J.AST.2017.08.032, 2017.

Dastanpour, R. and Rogak, S. N.: Observations of a correlation between primary particle and aggregate size for soot particles, Aerosol Sci. Technol., 48, 1043–1049, https://doi.org/10.1080/02786826.2014.955565, 2014.

Döpelheuer, A. and Lecht, M.: Influence of engine performance on emission characteristics, in: Symposium of the applied vehicle Technology Pane-Gas Turbine Engine Combustion, Emissions and alternative fuels, Lisbon, Portugal, 1998.

DuBois, D. and Paynter, G.: Fuel Flow Method2" for Estimating Aircraft Emissions, J. Aerosp., 115, 1–14, https://doi.org/https://doi.org/10.4271/2006-01-1987, 2006.

EASA: ICAO Aircraft Engine Emissions Databank (07/2021), https://www.easa.europa.eu/domains/environment/icao-aircraft-engine-emissions-databank, 2021. Last access: 17 August 2021

ECMWF: The Copernicus Programme: Climate Data Store, https://cds.climate.copernicus.eu/#!/home, 2021. Last access: 15 February 2022.

EUROCONTROL: User Manual for the Base of Aircraft Data (BADA) Family 4, 2016.

EUROCONTROL: User Manual for the Base of Aircraft Data (BADA) Revision 3.15, EUROCONTROL Experimental Centre (EEC), 2019.

European Environment Agency: 1.A.3.a Aviation 1 Master emissions calculator 2019, https://www.eea.europa.eu/publications/emep-eea-guidebook-2019/part-b-sectoral-guidance-chapters/1-energy/1-a-combustion/1-a-3-a-aviation-1/view, 2019. Last access: 25 August 2023.

Heathrow Airport: Traffic Statistics, https://www.heathrow.com/company/investor-centre/reports/traffic-statistics, 2022. Last access: 16 August 2022.

Hersbach, H., Bell, B., Berrisford, P., Hirahara, S., Horányi, A., Muñoz-Sabater, J., Nicolas, J., Peubey, C., Radu, R., Schepers, D., Simmons, A., Soci, C., Abdalla, S., Abellan, X., Balsamo, G., Bechtold, P., Biavati, G., Bidlot, J., Bonavita, M., De Chiara, G., Dahlgren, P., Dee, D., Diamantakis, M., Dragani, R., Flemming, J., Forbes, R., Fuentes, M., Geer, A., Haimberger, L., Healy, S., Hogan, R. J., Hólm, E., Janisková, M., Keeley, S., Laloyaux, P., Lopez, P., Lupu, C., Radnoti, G., de Rosnay, P., Rozum, I., Vamborg, F., Villaume, S., and Thépaut, J. N.: The ERA5 global reanalysis, Q. J. R. Meteorol. Soc., 146, 1999–2049, https://doi.org/10.1002/qj.3803, 2020.

IATA: Industry Statistics: Fact Sheet (June 2022), https://www.iata.org/en/iata-repository/pressroom/fact-sheets/industry-statistics/, 2022a. Last access: 15 August 2022.

IATA: Passenger Demand Recovery Continued in 2021 but Omicron Having Impact: https://www.iata.org/en/pressroom/2022-releases/2022-01-25-02/, 2022b. Last access: 17 August 2022.

ICAO: The World of Air Transport in 2019: https://www.icao.int/annual-report-2019/Pages/the-world-of-air-transport-in-2019.aspx, 2020. Last access: 15 August 2022.

ICAO: Overview of Automatic Dependent Surveillance-Broadcast (ADS-B) Out, https://www.icao.int/NACC/Documents/Meetings/2021/ADSB/P01-OverviewADSBOut-ENG.pdf, 2021a. Last access: 12 December 2022.

ICAO: The World of Air Transport in 2020, https://www.icao.int/annual-report-2020/Pages/the-world-of-air-transport-in-2020.aspx, 2021b. Last access: 15 August 2022.

ICAO: Air Transport Monitor: https://www.icao.int/sustainability/pages/air-traffic-monitor.aspx, n.d.. Last access: 7 September 2022.

Park, K., Kittelson, D. B., Zachariah, M. R., and McMurry, P. H.: Measurement of inherent material density of nanoparticle agglomerates, J. Nanoparticle Res., 6, 267–272, https://doi.org/10.1023/B:NANO.0000034657.71309.e6, 2004.

Peck, J., Oluwole, O. O., Wong, H.-W., and Miake-Lye, R. C.: An algorithm to estimate aircraft cruise black carbon emissions for use in developing a cruise emissions inventory, J. Air Waste Manage. Assoc., 63, 367–375, https://doi.org/10.1080/10962247.2012.751467, 2013.

Port Authority of New York and New Jersey: Airport Traffic Statistics, https://www.panynj.gov/airports/en/statistics-general-info.html, 2022. Last access: 16 August 2022.

Quadros, F. D. A., Snellen, M., Sun, J., and Dedoussi, I. C.: Global Civil Aviation Emissions Estimates for 2017–2020 Using ADS-B Data, J. Aircr., 1–11, https://doi.org/10.2514/1.C036763, 2022.

Savitzky, A. and Golay, M. J. E.: Smoothing and Differentiation of Data by Simplified Least Squares Procedures., Anal. Chem., 36, 1627–1639, https://doi.org/10.1021/ac60214a047, 1964.

Schripp, T., Anderson, B. E., Bauder, U., Rauch, B., Corbin, J. C., Smallwood, G. J., Lobo, P., Crosbie, E. C., Shook, M. A., Miake-Lye, R. C., Yu, Z., Freedman, A., Whitefield, P. D., Robinson, C. E., Achterberg, S. L., Köhler, M., Oßwald, P., Grein, T., Sauer, D., Voigt, C., Schlager, H., and LeClercq, P.: Aircraft engine particulate matter emissions from sustainable aviation fuels: Results from ground-based measurements during the NASA/DLR campaign ECLIF2/ND-MAX, 325, 124764, https://doi.org/10.1016/J.FUEL.2022.124764, 2022.

Schumann, U., Penner, J. E., Chen, Y., Zhou, C., and Graf, K.: Dehydration effects from contrails in a coupled contrail–climate model, Atmos. Chem. Phys., 15, 11179–11199, https://doi.org/10.5194/acp-15-11179-2015, 2015.

Singapore Airport: Statistics for Singapore Airport, https://singaporeairport.net/statistics/, 2022. Last access: 16 August 2022.

Sobieralski, J. B. and Mumbower, S.: Jet-setting during COVID-19: Environmental implications of the pandemic induced private aviation boom, Transp. Res. Interdiscip. Perspect., 13, 100575, https://doi.org/10.1016/J.TRIP.2022.100575, 2022.

Spire Aviation: Industry Leading ADS-B Data, https://insights.spire.com/spire-aviation-landing-page?utm_feeditemid=&utm_device=c&utm_term=aviation insights&utm_source=google&utm_medium=ppc&utm_campaign=Aviation+Data&hsa_cam=12065039426&hsa_grp=115763976669&hsa_mt=b&hsa_src=g&hsa_ad=533271178213&hsa_, n.d.. Last access: 22 December 2022.

Stettler, M. E. J., Boies, A., Petzold, A., and Barrett, S. R. H.: Global civil aviation black carbon emissions, Environ. Sci. Technol., 47, 10397–10404, https://doi.org/10.1021/es401356v, 2013.

Stickles, R. and Barrett, J.: TAPS II Combustor Final Report, General Electric, https://www.faa.gov/about/office_org/headquarters_offices/apl/research/aircraft_technology/cleen/reports/media/TAPS_II_Public_Final_Report.pdf, 2013. Last access: 12 December 2022.

Teoh, R., Stettler, M. E. J., Majumdar, A., Schumann, U., Graves, B., and Boies, A.: A methodology to relate black carbon particle number and mass emissions, J. Aerosol Sci., 132, 44–59, https://doi.org/10.1016/J.JAEROSCI.2019.03.006, 2019.

Teoh, R., Schumann, U., Majumdar, A., and Stettler, M. E. J.: Mitigating the Climate Forcing of Aircraft Contrails by Small-Scale Diversions and Technology Adoption, Environ. Sci. Technol., 54, 2941–2950, https://doi.org/10.1021/acs.est.9b05608, 2020.

Teoh, R., Schumann, U., Gryspeerdt, E., Shapiro, M., Molloy, J., Koudis, G., Voigt, C., and Stettler, M.: Aviation Contrail Climate Effects in the North Atlantic from 2016-2021., 22, 10919–10935, https://doi.org/https://doi.org/10.5194/acp-2022-169, 2022a.

Teoh, R., Schumann, U., Voigt, C., Schripp, T., Shapiro, M., Engberg, Z., Molloy, J., Koudis, G., and Stettler, M. E. J.: Targeted Use of Sustainable Aviation Fuel to Maximise Climate Benefits, Environ. Sci. Technol., 56, 17246–17255, https://doi.org/https://doi.org/10.1021/acs.est.2c05781, 2022b.

Voigt, C., Kleine, J., Sauer, D., Moore, R. H., Bräuer, T., Le Clercq, P., Kaufmann, S., Scheibe, M., Jurkat-Witschas, T., Aigner, M., Bauder, U., Boose, Y., Borrmann, S., Crosbie, E., Diskin, G. S., DiGangi, J., Hahn, V., Heckl, C., Huber, F., Nowak, J. B., Rapp, M., Rauch, B., Robinson, C., Schripp, T., Shook, M., Winstead, E., Ziemba, L., Schlager, H., and Anderson, B. E.: Cleaner burning aviation fuels can reduce contrail cloudiness, Commun. Earth Environ. 2021 21, 2, 1–10, https://doi.org/10.1038/s43247-021-00174-y, 2021.

Wasiuk, D. K., Lowenberg, M. H., and Shallcross, D. E.: An aircraft performance model implementation for the estimation of global and regional commercial aviation fuel burn and emissions, Transp. Res. Part D Transp. Environ., 35, 142–159, https://doi.org/10.1016/j.trd.2014.11.022, 2015.

Wikipedia: ICAO airport code: https://en.wikipedia.org/wiki/ICAO_airport_code, n.d.. Last access: 7 September 2022.